Article

Neuron

Stable Positioning of Unc13 Restricts Synaptic Vesicle Fusion to Defined Release Sites to Promote Synchronous Neurotransmission

Highlights

- Local Unc13 levels predict action-potential-evoked release at single AZs
- Unc13 generates and positions SV release sites
- SV-Ca^{2+} channel exclusion zone boundaries depend on Unc13 positioning
- Specific site positioning ensures efficient, temporally precise neurotransmission

Authors

Suneel Reddy-Alla, Mathias A. Böhme, Eric Reynolds, ..., Stefan W. Hell, Stephan J. Sigrist, Alexander M. Walter

Correspondence

stephan.sigrist@fu-berlin.de (S.J.S.), awalter@fmp-berlin.de (A.M.W.)

In Brief

Neurotransmission relies on synaptic vesicle release from unique sites. Reddy-Alla et al. now identify a function of Unc13A in release site generation and stable positioning with sub-active zone precision to ensure well-defined Ca^{2+} channel distances and adequate release probability.

Reddy-Alla et al., 2017, Neuron *95*, 1–15
September 13, 2017
http://dx.doi.org/10.1016/j.neuron.2017.08.016

CellPress

Please cite this article in press as: Reddy-Alla et al., Stable Positioning of Unc13 Restricts Synaptic Vesicle Fusion to Defined Release Sites to Promote Synchronous Neurotransmission, Neuron (2017), http://dx.doi.org/10.1016/j.neuron.2017.08.016

Neuron
Article

Stable Positioning of Unc13 Restricts Synaptic Vesicle Fusion to Defined Release Sites to Promote Synchronous Neurotransmission

Suneel Reddy-Alla,[1,8] Mathias A. Böhme,[1,2,3,8] Eric Reynolds,[1] Christina Beis,[1] Andreas T. Grasskamp,[2,3] Malou M. Mampell,[1] Marta Maglione,[1,2,3] Meida Jusyte,[2] Ulises Rey,[1,4] Husam Babikir,[1] Anthony W. McCarthy,[2] Christine Quentin,[1] Tanja Matkovic,[1] Dominique Dufour Bergeron,[1] Zeeshan Mushtaq,[2] Fabian Göttfert,[5] David Owald,[6] Thorsten Mielke,[7] Stefan W. Hell,[5] Stephan J. Sigrist,[1,3,9,*] and Alexander M. Walter[2,9,10,*]
[1]Institute for Biology/Genetics, Freie Universität Berlin, 14195 Berlin, Germany
[2]Leibniz-Forschungsinstitut für Molekulare Pharmakologie, 13125 Berlin, Germany
[3]NeuroCure Cluster of Excellence, Charité Universitätsmedizin, 10117 Berlin, Germany
[4]Department of Theory and Bio-systems, Max Planck Institute of Colloids and Interfaces, Science Park Golm, 14424 Potsdam, Germany
[5]Department of Nanobiophotonics, Max Planck Institute for Biophysical Chemistry, 37077 Göttingen, Germany
[6]Institut für Neurophysiologie, Charité Universitätsmedizin, 10117 Berlin, Germany
[7]Max Planck Institute for Molecular Genetics, 14195 Berlin, Germany
[8]These authors contributed equally
[9]Senior author
[10]Lead Contact
*Correspondence: stephan.sigrist@fu-berlin.de (S.J.S.), awalter@fmp-berlin.de (A.M.W.)
http://dx.doi.org/10.1016/j.neuron.2017.08.016

SUMMARY

Neural information processing depends on precisely timed, Ca^{2+}-activated synaptic vesicle exocytosis from release sites within active zones (AZs), but molecular details are unknown. Here, we identify that the (M)Unc13-family member Unc13A generates release sites and show the physiological relevance of their restrictive AZ targeting. Super-resolution and intravital imaging of *Drosophila* neuromuscular junctions revealed that (unlike the other release factors Unc18 and Syntaxin-1A) Unc13A was stably and precisely positioned at AZs. Local Unc13A levels predicted single AZ activity. Different Unc13A portions selectively affected release site number, position, and functionality. An N-terminal fragment stably localized to AZs, displaced endogenous Unc13A, and reduced the number of release sites, while a C-terminal fragment generated excessive sites at atypical locations, resulting in reduced and delayed evoked transmission that displayed excessive facilitation. Thus, release site generation by the Unc13A C terminus and their specific AZ localization via the N terminus ensure efficient transmission and prevent ectopic, temporally imprecise release.

INTRODUCTION

Neurotransmission across synapses relies on the precisely timed exocytosis of synaptic vesicles (SVs) at presynaptic active zone (AZ) membranes (Südhof, 2012). Action potentials (APs) activate presynaptic voltage-gated Ca^{2+} channels leading to fast and local elevation of intracellular Ca^{2+} concentrations that are sensed by the SV release machinery to induce SV fusion. Ca^{2+} sensing relies on the vesicular protein synaptotagmin, while the formation of SNARE complexes, composed of the vesicular protein synaptobrevin-2/VAMP2 and the plasma membrane (PM) proteins Syntaxin-1A (Syx-1A) and SNAP25, provide energy necessary for fusion (Jahn and Fasshauer, 2012). Before SV fusion can be evoked by APs, a number of well-coordinated reactions take place. Docking, the physical SV attachment to the PM, and priming, the maturation into a fusion competent state, require the concerted action of the SNAREs, Unc13, and Unc18 (Jahn and Fasshauer, 2012; Rizo and Xu, 2015).

Pioneering analyses of the statistical features of neurotransmitter (NT) release established that exocytosis occurs from few highly specialized release sites (McLachlan, 1978; Vere-Jones, 1966; Zucker, 1973). Theoretical calculations further suggested that a well-defined placement of SV release sites relative to Ca^{2+} channels is required for effective transmission and proper short-term plasticity (Keller et al., 2015; Meinrenken et al., 2002; Nakamura et al., 2015). To address the physiological relevance of release site placement experimentally, it would be useful to alter release site localization selectively, but the relevant release site generating molecule is yet unknown. AZ scaffolding proteins like RIM, Bruchpilot (BRP)/ELKS, and Rim-binding protein (RBP) regulate SV docking and release site numbers and positions (Acuna et al., 2015; Han et al., 2011; Matkovic et al., 2013; Müller et al., 2012; Tang et al., 2016; Wang et al., 2016). But as none of these proteins have an established direct function in SV fusion, the question arises which downstream effector establishes release sites at AZ scaffolds.

Release sites are locations where SVs dock and prime for release; thus, release site defining molecules are expected to function in these reactions. Their localization should predict SV

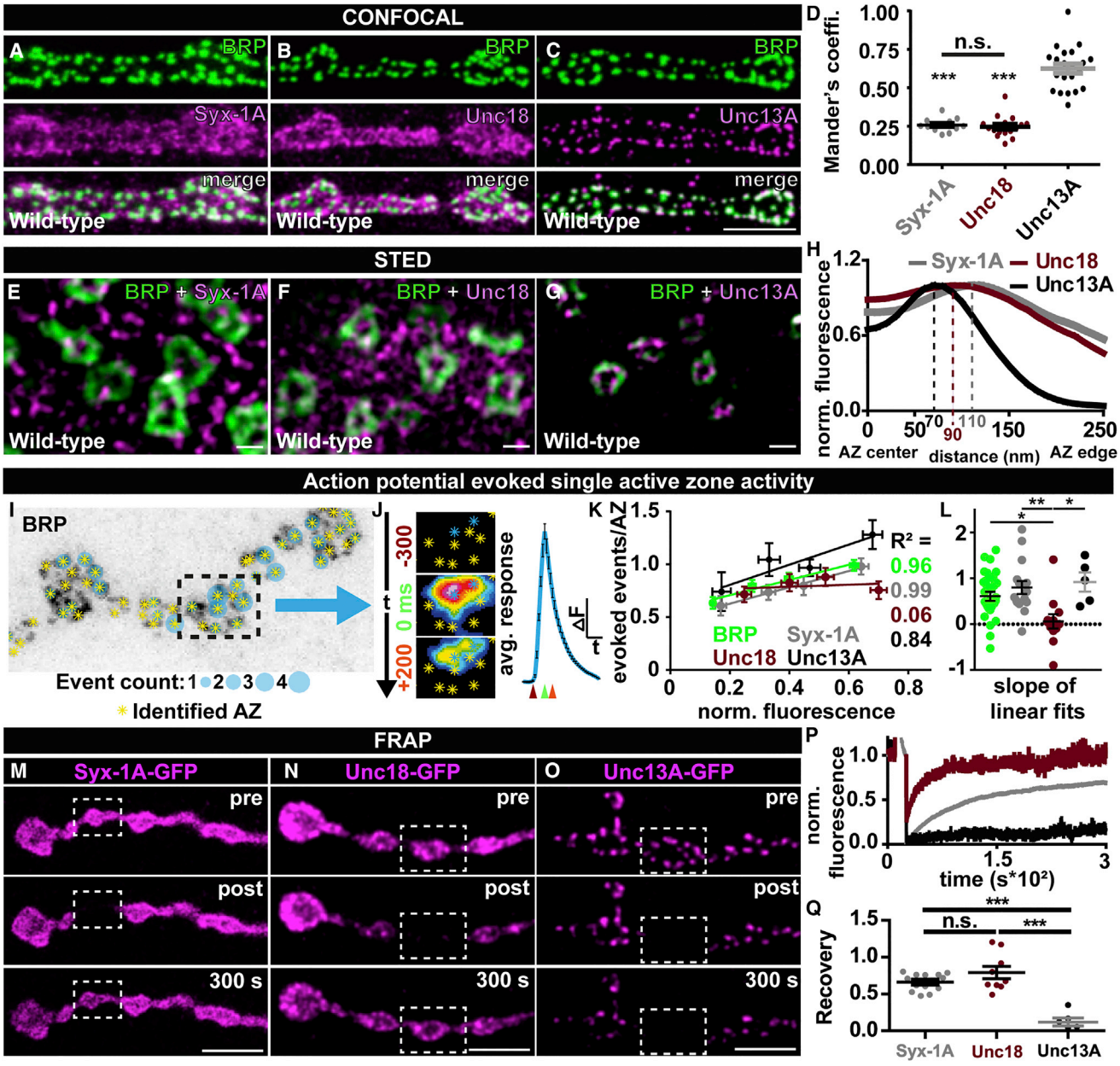

Figure 1. Unc13A Specifically Localizes at AZs, Predicts AZ Activity, and Recovers Slower than Unc18 or Syx-1A

(A–C) Wild-type muscle 4 NMJs of segment A2–4 from third-instar larvae labeled with indicated antibodies recognizing BRP (green) and Syx-1A (A; magenta), Unc18 (B; magenta), or Unc13A (C; magenta).

(D) Mander's overlap coefficient for Syx-1A/Unc18/Unc13A with BRP.

(E–G) Two-color STED images of AZs from third-instar wild-type larvae stained with indicated antibodies recognizing BRP (green) and Syx1-A (E; magenta), Unc18 (F; magenta), or Unc13A (G; magenta; data for Unc13A taken from Böhme et al., 2016).

(H) Mean intensity profile of Unc13A, Syx-1A, and Unc18 immunoreactivity plotted from the center of the AZ (reference: center of the BRP ring). Average intensity maxima of Unc13A, Unc18, and Syx-1A were found at 70, 90, and 110 nm from the AZ center, respectively (data for Unc13A taken from Böhme et al., 2016).

(I) Inverted confocal image of BRP after GCaMP recording, overlay: positions of identified AZs (yellow asterisks); size of blue dots indicates number of AP-evoked release events during recording.

(J) Left: time sequence (300 ms before, at the time of [0 ms], and 200 ms after the peak intensity) of GCaMP images in the sub-region indicated by a dashed rectangle in (I) (blue asterisks indicate AZ activity) (top to bottom). Right: average GCaMP fluorescence per AZ during a release event (scale bar, 200 a.u./400 ms).

(K) Average event counts plotted against the corresponding binned, normalized fluorescence of indicated AZ proteins, with linear fits and coefficient of determination.

(L) Linear fit slopes in individual measurements.

(legend continued on next page)

docking sites, and because estimated Ca^{2+} channel/release site distances are smaller than typical AZ dimensions they should localize within AZs with nanometer precision (Eggermann et al., 2011). Furthermore, because SV fusion at release sites occurs in an all or none fashion, synaptic transmission obeys binomial statistics and fluctuation analyses can be used to estimate the number of release sites (Clements and Silver, 2000; Vere-Jones, 1966; Zucker, 1973). Because this depends on the repetitive re-use of a fixed number of release sites (Neher, 2010), molecules generating these sites are expected to show high positional stability. Moreover, synaptic activity is expected to scale with the number of release sites. Therefore, a positive relation of the single AZ activity status on the limiting molecules generating release sites is expected. Ultimately, release site generating molecules will be revealed by mutation of candidate proteins that cause changes in release site number, position, or functionality. A dependence of synaptic transmission on the AZ-specific localization was suggested for the SV docking and priming factor Unc13, making it a prime candidate (Böhme et al., 2016; Hu et al., 2013; Kawabe et al., 2017; Zhou et al., 2013).

Using super-resolution (stimulated emission depletion [STED]) microscopy and intravital live imaging of glutamatergic *Drosophila* neuromuscular synapses, we found that Unc13A stably localized to AZs where it displayed turnover times of several hours. In contrast, the other essential SV docking and priming proteins Syx-1A and Unc18 were broadly distributed and exchanged within minutes. Local Unc13A levels predicted spontaneous and AP-evoked synaptic transmission at single AZs, and, while the same was true for local BRP levels, this scaffold dependence was weakened upon Unc13A knockdown, arguing that AZ scaffolds indirectly regulate activity and release site numbers by recruiting Unc13s. An N-terminal Unc13A fragment stably anchored in the same AZ-subregions as the full-length protein. Its overexpression in a wild-type background partially displaced endogenous Unc13A and reduced the number of release sites, in line with blocking interaction sites required to generate release sites at the AZ scaffold. In contrast, deletion of the N-terminal sequence resulted in promiscuous and transient localization of the remaining protein, similar to Unc18 and Syx-1A. Synaptic transmission operating via this C-terminal fragment displayed increased spontaneous but decreased AP-evoked activity. Furthermore, although the number of release sites was dramatically increased, their release probability was so low that even extreme Ca^{2+} influx only activated few of them. Ultra-structural analysis of AZs expressing the C-terminal fragment revealed increased but unspecific SV docking. An exclusion zone of docked SVs close to the AZ center (where Ca^{2+} channels reside), which was clearly established in control cells, was lost. Responses to high-frequency trains showed extreme facilitation and delayed release building up during the train, indicative of release sites atypically distant from Ca^{2+} channels, as effects were reverted by the Ca^{2+} buffer EGTA. Thus, the Unc13A N- and C-terminal portions function in stable AZ positioning (via AZ scaffold interactions) and release site generation at well-defined sub-AZ positions to ensure temporal fidelity and adequate short-term plasticity of synaptic transmission.

RESULTS

SV release sites are defined locations where SVs dock and prime for release. To identify molecules defining these sites, we therefore focused on the essential docking and priming factors Syx-1A, Unc18 (flybase: Rop), and Unc13A, the Unc13 isoform dominating evoked SV release at *Drosophila* neuromuscular junction (NMJ) synapses (flybase: unc-13) (Böhme et al., 2016; Schulze et al., 1994, 1995). First, we analyzed which of these were kept within a narrow sub-AZ distribution range, as expected from release sites (Eggermann et al., 2011). Co-staining Unc13A, Syx-1A, and Unc18 with the AZ marker BRP revealed highly specific AZ localization of Unc13A (Figure 1C; Böhme et al., 2016), but this feature was neither shared by Syx-1A nor Unc18 (Figures 1A–1D), in agreement with observations in other systems (Pertsinidis et al., 2013; Wilhelm et al., 2014). We also investigated sub-AZ specific localization using STED microscopy (lateral resolution of ~40 nm), which revealed typical ring-like BRP structures (Figures 1E–1G, green). Unc13A predominantly localized within the BRP-ring but Syx-1A and Unc18 positive signals appeared non-specifically distributed at and in-between AZs (Figures 1E–1G). Previous STED analyses established that the voltage-sensitive N/P/Q-type Ca^{2+} channel $\alpha 1$ subunit Cacophony (Cac; exclusively mediating evoked release at the *Drosophila* NMJ) localizes to the center of the BRP ring, which can thus be used as a proxy for voltage-gated Ca^{2+} channel locations (Fouquet et al., 2009; Kawasaki et al., 2004; Liu et al., 2011). To quantitatively compare local protein distributions and their respective distance to the Ca^{2+} channels in the AZ center, we calculated mean fluorescence profiles across many aligned AZs (see STAR Methods). Unlike the highly specific Unc13A localization (Böhme et al., 2016), fluorescence profiles of Unc18 and Syx-1A were fairly flat (Figure 1H), indicating rather uniform protein distributions throughout AZs with only minor enrichment 90 and 110 nm from the AZ center, respectively.

Because the number of release sites limits synaptic transmission, single AZ activities should positively correlate with the local levels of proteins that are limiting reagents for their generation. We investigated this at *Drosophila* larval NMJ AZs (which are intrinsically heterogeneous regarding their activity and protein levels) by imaging of a post-synaptically expressed fluorescent Ca^{2+} indicator (GCaMP) that enables visualization of presynaptic release events with single SV resolution (Melom et al., 2013; Newman et al., 2017). AZ activities during AP stimulation

(M–O) FRAP of motoneuronally overexpressed Syx-1A-GFP (M), Unc18-GFP (N), and Unc13A-GFP (O) of muscles 26/27. Dashed box shows bleached bouton before (pre), immediately after (post), and 300 s after bleaching.

(P) Fluorescence recovery as a function of time.

(Q) Quantification of fluorescence recovery after 300 s. Figure source data, number of experiments, and p values: see Table S1.

Scale bar in (A)–(C) and (M)–(O), 5 μm, and in (E)–(G), 200 nm. Statistics (D, L, and Q): one-way analysis of variance (ANOVA) tests, followed by a Tukey's multiple-comparison test. *$p \leq 0.05$; **$p \leq 0.01$; ***$p \leq 0.001$; ns, not significant, $p > 0.05$. All panels show mean ± SEM. For further details, see Figure S1.

(36 APs at 0.2 Hz) were imaged, the larvae fixed and co-stained against BRP (to recognize AZs) together with Unc13A, Unc18, or Syx1A (Figures 1I–1L). Aligning these stainings to live movies allowed us to quantify how often individual AZs were active in relation to local protein levels (Figures 1K and 1L; Movie S1). In line with previous analyses, we found strong correlations of AP evoked AZ activities with local BRP levels (Muhammad et al., 2015; Peled et al., 2014). Furthermore, activities correlated strongly with local Unc13A and Syx-1A levels, but not with those of Unc18 (Figures 1K and 1L).

Because the number of release sites per synapse is constant (Neher, 2010), a stable AZ localization of release site defining proteins is expected. We therefore quantified the *in vivo* mobility of GFP-tagged Unc13A, Syx-1A, and Unc18 by measuring fluorescence recovery after photobleaching (FRAP). Importantly, these GFP-fusion proteins were found at positions typical for the endogenous proteins in live imaging experiments of anesthetized larvae (compare Figures 1A–1C and 1M–1O). After imaging baseline fluorescence (Figures 1M–1O, "pre"), single boutons were bleached with high laser power, leading to very low fluorescence post bleaching (Figures 1M–1P, "post"). While fluorescence recovered within few minutes in the cases of Unc18-GFP and Syx-1A-GFP, Unc13A-GFP fluorescence showed essentially no recovery in the same time frame (Figures 1M–1Q, "300 s"). In fact, its recovery was so slow, that its time constant of ~7 hr could only be measured in repeated imaging sessions (Figures S1A and S1B). Taken together, we find that only Unc13A shares all features expected for a release site generating molecule: it has well-defined, stable sub-AZ localization and is a local predictor of AZ-activity.

AZ-Scaffold-Dependent Unc13A Recruitment Determines the Functional AZ Status

That AZ-scaffold sizes predict the propensity to engage in AP-evoked synaptic activity was previously described (Holderith et al., 2012; Muhammad et al., 2015; Peled et al., 2014). To understand whether this relation is exclusive to evoked transmission or whether it extends to AP-independent spontaneous activity, we performed experiments where spontaneous AZ activities were first imaged for 100 s without stimulation before APs were elicited to stimulate release from the same set of AZs (Figure S2A). Both transmission modes induced similar postsynaptic activation (Figure S2B; GCaMP amplitudes: spontaneous [spont.]: 677.1 ± 18.6 arbitrary units [a.u.]; evoked: 682.8 ± 18.8 a.u.; mean ± SEM; $p = 0.9378$, Mann-Whitney U test) and occurred from overlapping as well as from distinct AZs during our observation time (Figures S2A and S2E). This agrees with previous findings (Melom et al., 2013; Muhammad et al., 2015). Interestingly, and unlike reported for spontaneous AZ activity in *Drosophila* null mutants of the SV GTPase Rab3 (Peled et al., 2014), spontaneous activity tracked with postsynaptic GCaMP in a wild-type background was highly positively correlated to local BRP levels (Figures S2C and S2D). As was the case for AP-evoked transmission, spontaneous activity also scaled linearly with local Unc13A levels (Figures S2C and S2D), suggesting a dependence of both transmission modes on BRP/Unc13A.

Because both BRP and Unc13A levels predicted the functional AZ status, we next investigated their causal relationship. Unc13A directly interacts with BRP (Böhme et al., 2016), and its AZ levels scale proportionally to BRP (Figure 2A). Thus, BRP may affect release indirectly, by recruiting Unc13A to generate release sites. If this were the case, we would expect Unc13A manipulation to alter the coupling between AZ-scaffold size (i.e., BRP levels) and its release status. This we tested by RNAi-mediated Unc13A knockdown (KD) in motoneurons, which reduced Unc13A levels, but did not affect postsynaptic (GCaMP) activation by SV release in either transmission mode (Figures 2A and 2C). Analysis of the *unc13A*^{null} phenotype in conventional electrophysiological recordings revealed increased spontaneous transmission and decreased AP-evoked release (Böhme et al., 2016), and we saw similar tendencies at single AZs following Unc13A knockdown (Figures 2B and 2D). Moreover, the activity profile of AZs dedicated to specific transmission modes shifted and a larger AZ fraction was exclusively active spontaneously during our recordings (Figure 2G). Importantly, Unc13A knockdown weakened the relationship between the AZ levels of Unc13A and BRP (Figure 2A), allowing us to test whether this impaired Unc13A recruitment weakened the relation between AZ activity and BRP levels. Indeed, the predictive value of BRP levels for the AZ activity status was reduced in both transmission modes (Figures 2E and 2F), arguing that the correlation between AZ activity and AZ size depends on scaffold-mediated Unc13A recruitment to generate release sites.

Precise and Stable Unc13 AZ Localization Depends on Its N Terminus

The two *Drosophila* Unc13 isoforms, Unc13A and Unc13B, localize differentially within single AZs (Böhme et al., 2016). They differ in their N-terminal parts but harbor identical C-terminal halves containing the MUN domain essential for vesicle priming (Basu et al., 2005), suggesting a crucial function of the N termini in protein localization. This agrees with observations in other systems: at mammalian and *C. elegans* AZs, (M)Unc13 localization depends on an N-terminal C2A domain (Deng et al., 2011; Hu et al., 2013; Zhou et al., 2013). Although the C2A domain is lacking in *Drosophila* Unc13A, its N terminus directly binds BRP (Böhme et al., 2016), and it was recently shown that the BRP homolog ELKS recruits bMunc13-2 (which also lacks the C2A domain) to AZs of mammalian synapses (Kawabe et al., 2017).

To investigate the vertical orientation of Unc13A domains at the AZ, we analyzed STED images of immunostainings labeling a C-terminal BRP epitope (known to face away from the PM; Fouquet et al., 2009) together with antibodies recognizing different Unc13A epitopes (Figure 3B). Vertical fluorescence intensity profiles in the different channels were aligned to the BRP signal and then averaged over all investigated AZs (see STAR Methods for details). Our analysis revealed average intensity maxima of stainings against the Unc13A N-terminal-, C-terminal MUN domain), and GFP epitopes at ~20, ~30, and ~70 nm from the BRP C terminus (Figure 3A). Furthermore, the C-terminal GFP-tag localized to similar positions as the C terminus of RBP, which was previously shown to be close to the PM (Figure 3A) (Liu et al., 2011). We thus suggest a slightly elongated structure of Unc13A, with its C-terminal domains facing toward the PM.

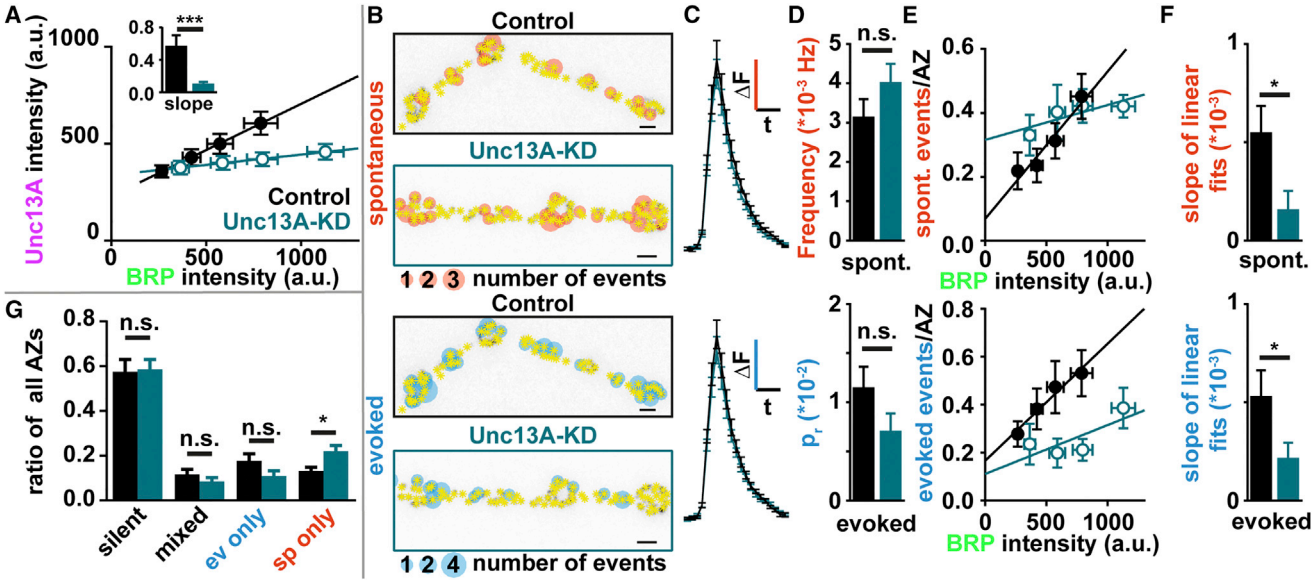

Figure 2. AZ BRP Levels Predict Single AZ Activity in an Unc13A-Dependent Manner

(A) Absolute Unc13A AZ levels are correlated to local BRP amounts. RNAi-mediated knockdown of Unc13A in motoneurons reduces Unc13A levels, leading to a reduction in the slope (inset). In all figure panels: control: black; Unc13A-RNAi: turquoise (B–F) analysis of spontaneous (top line) and evoked (bottom line) single AZ activities.

(B) Single AZ activity maps showing inverted BRP immunostaining overlaid with identified AZs (asterisks) and circles corresponding in size to the number of observed events.

(C) Comparison (cell-wise) of mean quantal postsynaptic GCaMP5 signals linked to AZ activity.

(D) Single AZ spontaneous event frequency (top) and AZ release probability (bottom) in both genotypes.

(E) Relation of single AZ activity to BRP levels.

(F) Cell-wise comparison of slopes from linear fits to cell-wise data as shown in (E) reveals a weakening in the relation of AZ activity to local BRP following Unc13A knockdown.

(G) Relative fraction of AZs with specific activity patterns. Silent, no activity; mixed, spontaneous and evoked; ev only, only evoked; sp only, only spontaneous. Figure source data, number of experiments, and p values: see Table S1.

Scale bar in (B), 2 μm, and in (C), 250 a.u., 500 ms. Statistics: t test except for inset in (A) where a Mann-Whitney U test was used. ***$p \leq 0.001$; *$p \leq 0.05$; not significant, $p > 0.05$. All panels show mean ± SEM. For further details, see Figure S2.

To investigate the function of different Unc13A portions, we generated two GFP-tagged Unc13A fragments: N-term-GFP and C-term-GFP (Figure 3B). Full-length Unc13A-GFP served as a control (Figures 1O and 3B). Confocal and STED analysis revealed that the N-term-GFP fragment overexpressed in wild-type localized to similar locations as the control and endogenous protein (Figures 1C, 3C, 3D, and 3F; Figures S3A and S3B). Fluorescence signals of N-term-GFP were weaker than those of full-length Unc13A-GFP, potentially attributable to a decreased stability (Figures S3C–S3F). In contrast, the C-terminal fragment displayed higher levels (Figures S3G–S3I). However, its localization appeared unspecific (i.e., no longer confined to AZs), which was confirmed by markedly reduced values of Mander's overlap coefficient (Figures 3E and 3F) and STED analysis (Figures S3J and S3K). We also investigated the stability of the two protein fragments by assaying FRAP. The lower expression levels of the N-term-GFP fragment (Figures S3C–S3F) required higher laser powers for live imaging, which often resulted in the unwanted bleaching of the signal throughout the NMJ. We therefore resorted to shorter acquisition times and only imaged at 30-s intervals in this case. FRAP analysis revealed a very stable positioning of the N-term-GFP fragment, similar to that of the full-length protein (Figures 3G, 3H, 3J, and 3K). In contrast, fluorescence of the C-term-GFP fragment recovered quickly, suggesting short residence (few minutes), similar to Syx-1A and Unc18 (compare Figures 3I–3K with Figures 1M–1Q). Thus, by characterizing N- and C-terminal Unc13A fragments, we identify an essential role of the N terminus for protein localization and long-term AZ anchoring.

Overexpression of the N-Term-GFP Fragment Blocks Some SV Release Sites

We next attempted the expression of either fragment in the absence of all Unc13 isoforms. Loss of *unc13* results in early embryonic lethality (Aravamudan et al., 1999), which was rescued by pan-neuronal expression of either Unc13A-GFP or the C-term-GFP fragment, but not by that of the N-term-GFP fragment, suggesting it cannot maintain synaptic transmission despite proper localization. The lethality of this genotype prevented further analysis. Instead, we investigated possible dominant negative effects of N-term-GFP overexpression in the wild-type background. Because the Unc13A N terminus directly interacts with BRP/RBP *in vitro* (Böhme et al., 2016), we speculated that the N-term-GFP fragment interferes with the AZ recruitment of

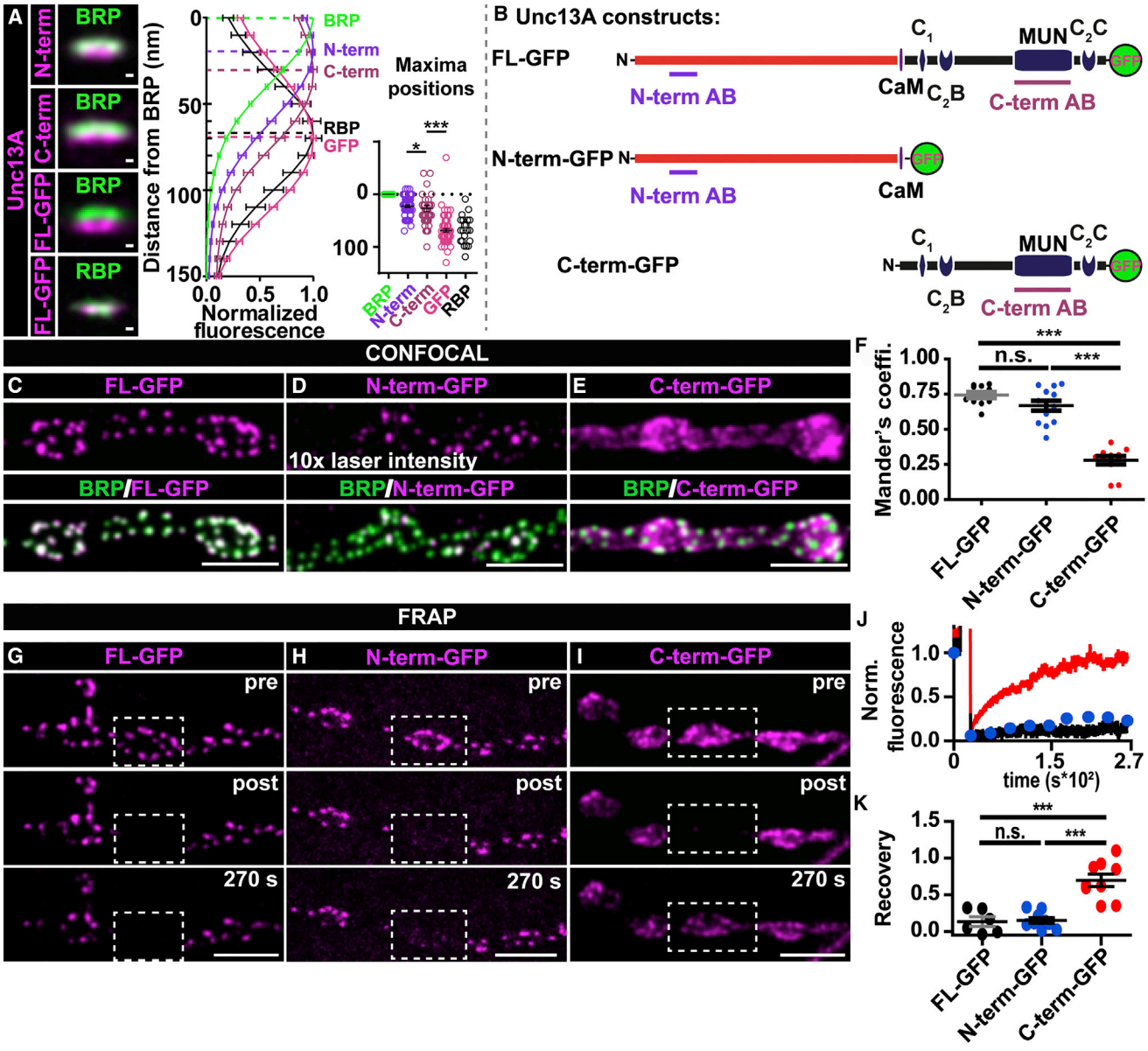

Figure 3. The Unc13A N Terminus Is Essential for AZ Localization and Long-Term Stabilization

(A) Left: average two-color STED images of AZs in side view (cytoplasm top; PM bottom) from third-instar wild-type larvae stained with indicated antibodies. (For FL-GFP see also B). Right: normalized fluorescence profile of BRP (green), RBP (black), and three distinct portions of Unc13A (the N terminus [N-term: purple], the C terminus [C-term: brown; recognizes MUN domain], and the C-terminal GFP-tag [GFP: magenta]) aligned to the peak of BRP intensity. Dot plot shows the quantification of the distances between the intensity maxima of the BRP profile and that of the investigated epitope for each AZ.

(B) Schematics of GFP-tagged constructs: full-length Unc13A (FL-GFP), N-term-, and C-term-GFP. Domains indicated: CaM, calmodulin; C1, C2B, C2C, and the MUN domain. Antibody (AB) epitopes are indicated.

(C–E) Muscle 4 NMJs of segments A2–A4 from third-instar larvae motoneuronally overexpressing Unc13A constructs: full-length Unc13A-GFP (C; FL-GFP), the N-term-GFP fragment (D), or the C-term-GFP fragment (E) labeled with antibodies recognizing BRP (green) and GFP (magenta).

(F) Mander's overlap coefficient for FL-GFP/N-term-GFP/C-term-GFP with BRP.

(G–I) FRAP of motoneuronally overexpressed FL-GFP (G), N-term-GFP (H), and C-term-GFP (I) at muscles 26/27. Dashed box shows bleached bouton before (pre), directly after (post), and 270 s after fluorescence bleaching.

(J and K) Mean, normalized fluorescence recovery for FL-GFP, N-term-GFP and C-term-GFP (J), and quantification of fluorescence recovery after 270 s (K). Images in (G) and FRAP traces of the FL-GFP in (J) are reproduced from Figure 1. Figure source data, number of experiments, and p values: see Table S1. Scale bar in (A), 50 nm, and in (C–E) and (G–I), 5 μm. Statistics: (A) Mann-Whitney U test (F and K): one-way analysis of variance (ANOVA) tests, followed by a Tukey's multiple-comparison test. *$p \leq 0.05$; ***$p \leq 0.001$; ns, not significant, $p > 0.05$. All panels show mean ± SEM. For further details, see Figure S3.

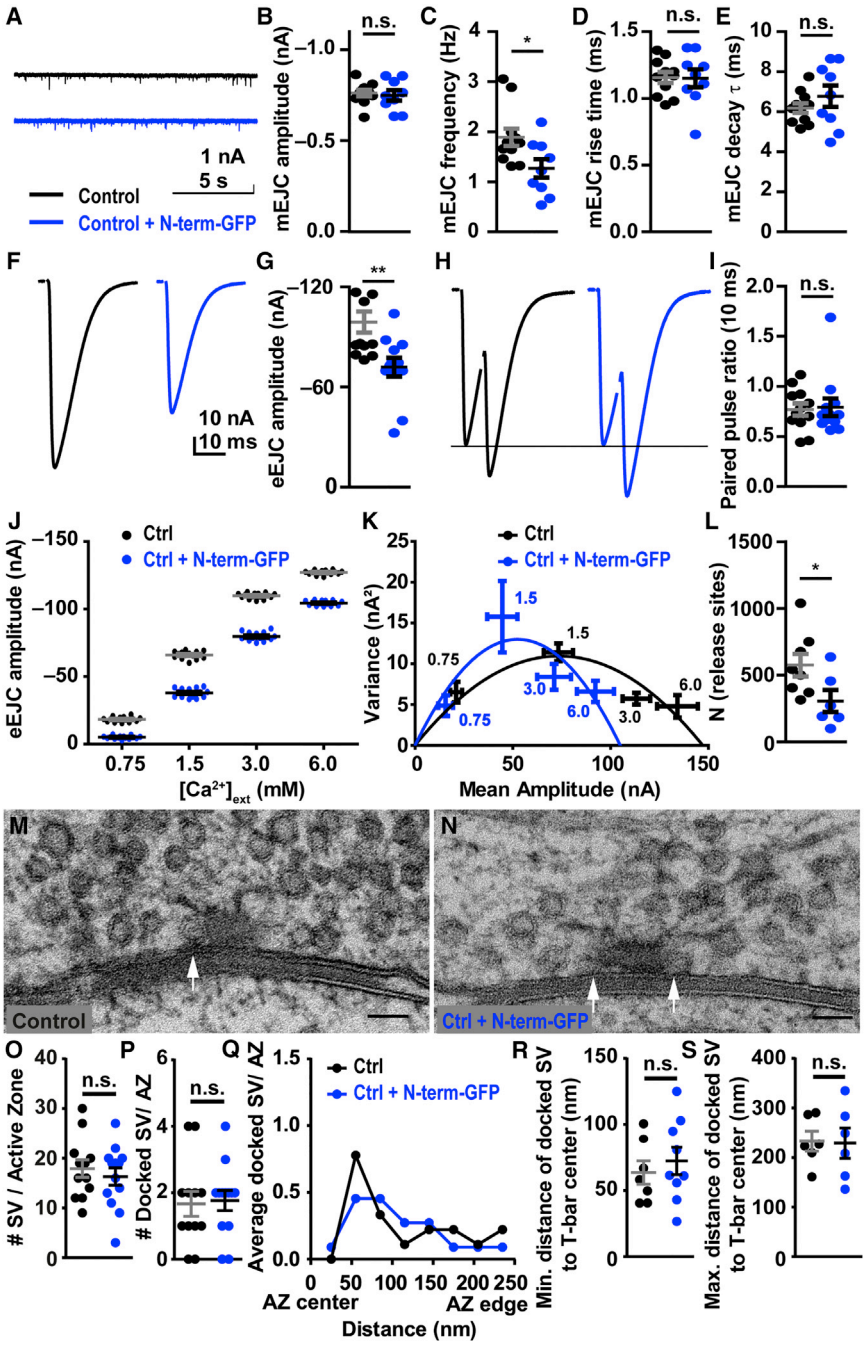

Figure 4. Overexpressing the Unc13 N Terminus Blocks SV Release Sites

Analysis of synaptic transmission and AZ ultrastructure in control larvae (black) and ones motoneuronally overexpressing the Unc13A N-term-GFP fragment (Ctrl + N-term-GFP, blue).

(A) Representative mEJC traces.

(B–E) Quantification of mEJC amplitudes (B), frequencies (C), rise times (D; 10% to 90%), and decay times (E).

(F and G) Representative eEJC traces (F) and quantification (G).

(H) Normalized representative paired-pulse eEJC traces with 10 ms ISI.

(I) Quantification of paired-pulse ratios. Recordings in (A)–(I) were performed in the presence of 1.5 mM extracellular Ca^{2+}.

(J) Scatterplot of eEJC amplitudes at indicated extracellular Ca^{2+} concentrations ($[Ca^{2+}]_{ext}$) from single representative Control or N-term-GFP-overexpressing cells.

(K) Variance-mean relationship in both genotypes. Average mean amplitudes and average variances at the indicated $[Ca^{2+}]_{ext}$. Lines represent best fit parabolas to the full dataset of either genotype.

(L) Average number of release sites (N) from cell-wise estimation.

(M and N) HPF-EM micrographs of AZs in the control condition (M) and upon over-expression of the GFP-tagged N-terminal Unc13A fragment (N). Docked SVs are indicated with white arrows.

(O and P) Number of total (O) and docked (P) SVs per AZ.

(Q) Average number of docked SVs within certain bins of distances from the T-bar center.

(R and S) Minimal (R; Min.) and maximal (S; Max.) distance of docked SVs to the T-bar pedestal center per AZ.

Figure source data, number of experiments and p values: see Table S1.

Scale bar in (M) and (N), 50 nm. Statistics: t test for (B)–(E), (G), (I), and (L) and Mann-Whitney U test for (O), (P), (R), and (S). *$p \leq 0.05$; **$p \leq 0.01$; ns, not significant, $p > 0.05$. All panels show mean ± SEM. For further details, see Figure S4.

endogenous Unc13A by competitive binding to the AZ scaffold. We verified this displacement by immunostaining for the MUN domain, revealing ~50% lower levels of endogenous Unc13A compared to controls (Figures S4A–S4C). Synaptic transmission in these flies was investigated by two electrode voltage clamp recordings. To achieve high motoneuronal overexpression of the N-term-GFP fragment we used a strong driver (OK371-Gal4). Recordings of postsynaptic miniature excitatory junctional currents (mEJCs) in the absence of stimulation were used to investigate the spontaneous release of individual SVs and revealed unaltered mEJC amplitudes and kinetics, but significantly lower mEJC frequencies compared to driver controls (Figures 4A–4E). AP-evoked release was studied by efferent nerve stimulation and revealed similarly reduced evoked excitatory junctional currents (eEJCs) (Figures 4F and 4G). We then tested whether overexpression of the N-term-GFP fragment affected the probability for evoked SV fusion (release probability) by probing synaptic short-term plasticity in response to AP-pairs given at 10-ms intervals (paired-pulse protocol, Figure 4H). We found no effect of Unc13A N-term-GFP overexpression on paired-pulse ratios (PPRs), suggesting identical release probabilities (Figures 4H and 4I).

To investigate whether the displacement of endogenous Unc13A via the N-term-GFP fragment affected the number

("N") of release sites, we performed fluctuation analysis (Clements and Silver, 2000). To determine N, the magnitudes of synaptic responses were altered and their variances tracked. This was achieved by repeatedly measuring AP-evoked synaptic transmission at increasing extracellular Ca^{2+} concentrations (Figure 4J). At low extracellular Ca^{2+} concentrations, only few release sites engage in transmission resulting in low variance. The variance then increases with increasing release due to the engagement of more sites but decreases again once the majority of sites becomes activated (Figures 4J and 4K), due to the binomial nature of the process. This results in a parabolic behavior of variances as a function of mean release amplitudes, and fitting a parabola to the data allows the calculation of N (Clements and Silver, 2000) (Figures 4K and 4L). Comparing N to control cells, we found that N-term-GFP overexpression significantly reduced the number of release sites participating in synaptic transmission (Figure 4L).

To test whether N-term-GFP overexpression affected SV docking, we performed ultra-structural analysis of AZs using high-pressure freeze (HPF) tissue conservation, which is best to maintain SV distributions (Imig et al., 2014). Electron microscopy (EM) micrographs revealed similar numbers of total and membrane docked SVs (touching the PM) (Figures 4M–4P). We also investigated the lateral distance of docked SVs from the center of the electron dense cytomatrix, which is largely composed of BRP and termed "T-bar" due to its shape. Because the voltage-gated Ca^{2+} channels in planar projected AZs fall into the center of the BRP scaffold (Fouquet et al., 2009; Liu et al., 2011), this distance can be used to estimate SV-Ca^{2+} channel distances (Böhme et al., 2016). While this distribution clearly peaked at distances around 50 nm from the AZ center in controls, we found a trend toward fewer docked SVs at this location upon N-term-GFP overexpression (Figure 4Q). Although this difference was not statistically significant, it qualitatively matches the 20%–30% reduction of synaptic transmission in this genotype (Figure 4G).

Our data suggest that the displacement of endogenous Unc13A from AZs by the N-term-GFP fragment reduces the number or the accessibility of release sites and indicates that the Unc13A C terminus (which is lacking in this fragment) is required for release site formation.

Unc13A Lacking Its N Terminus Generates Excessive Release Sites in Atypical Locations

We then tested whether the C-term-GFP fragment is sufficient for release site generation by pan-neuronal expression of the construct in *unc13*^{null} flies. mEJCs exhibited similar amplitudes but showed increased frequencies and rise times (10%–90% of the amplitude) compared to controls (expressing Unc13A-GFP in the *unc13*^{null}; Figures 5A–5D). mEJC decay time courses were similar (Figure 5E). In contrast to the experiments with the N-term-GFP fragment, where mEJC frequencies and evoked activities changed unidirectionally (i.e., a reduction of both, Figures 4C and 4G), NMJs rescued with the C-term-GFP construct had increased mEJC frequencies but suffered from reduced AP-evoked transmission (Figures 5A, 5C, 5F, and 5G), in agreement with recent observations in mouse hippocampal neurons (Liu et al., 2016). Release driven by the C-term-GFP fragment showed atypical paired-pulse facilitation compared to controls, in line with the contribution of low release probability release sites (Figures 5H and 5I). We could exclude that this phenotype was due to the loss of the Unc13A Calmodulin (CaM)-binding domain (which is lacking in the C-terminal fragment), because mutation predicted to disrupt CaM binding (Junge et al., 2004) had opposite effects: reduced mEJC frequencies, increased eEJC amplitudes, and decreased PPRs (Figure S5).

To investigate the relevance of stable and precise Unc13A AZ positioning for release site function, we analyzed the variance-mean relationship (Figures 5J and 5K). Strikingly, while control cells obeyed the expected parabolic behavior, this was not the case in animals rescued with the C-term-GFP fragment (Figure 5K). In fact, even increasing extracellular Ca^{2+} to extreme concentrations of 12 mM (beyond which recordings were not feasible) did not result in a decrease of synaptic variance and the relationship was better described by a line than by a parabola (Figure 5K; distinguished by Akaike's information criterion). A linear relation between variance and mean synaptic transmission indicates an extreme case of the binomial process with very low release probability and large N that approaches a Poisson distribution (Del Castillo and Katz, 1954; Vere-Jones, 1966). Our data thus indicate that the Unc13 C-terminal fragment is indeed able to generate release sites and does so in excessive numbers. These sites, however, suffer from an overall low release probability and fall behind the performance of wild-type synapses, which maintain more efficient transmission from fewer sites of higher release probability.

In agreement with the existence of more release sites, EM micrographs revealed an increase in docked SVs at AZs rescued with the C-terminal fragment (Figures 5M–5P). These docked SVs, however, were less specifically positioned (Figure 5Q), in line with the less specific localization of the C-term-GFP fragment (Figure 3; Figure S3). The distribution of distances to the AZ center was flattened, and an SV exclusion zone for distances below 50 nm, which was established in control cells (Keller et al., 2015), was lost (Figure 5Q). This resulted in shorter minimal distances of docked SVs to the AZ center (Figure 5R). Furthermore, there was a clear trend toward increased maximal distances of docked SVs to the AZ center (Figure 5S). Our data show that re-distribution of the Unc13 C-terminal fragment results in a similar redistribution of docked SVs, pointing toward a fundamental function of Unc13A in release site generation and positioning.

We also investigated whether the localization of other proteins involved in SV release was affected at AZs rescued with the C-term-GFP fragment. In confocal analyses, we found no change in the relative distributions of Syx-1A and Unc18, but a small yet significant increase of RBP levels outside of AZ regions, possibly indicative of a partial redistribution of core AZ components to release sites generated by the Unc13 C-terminal fragment (Figure S6).

The Unc13 N Terminus Precisely Positions Release Sites to Synchronize Transmission

The aberrant localization of release sites generated by the C-term-GFP fragment provides the unique opportunity to study the consequence of uncoupling release sites from the AZ

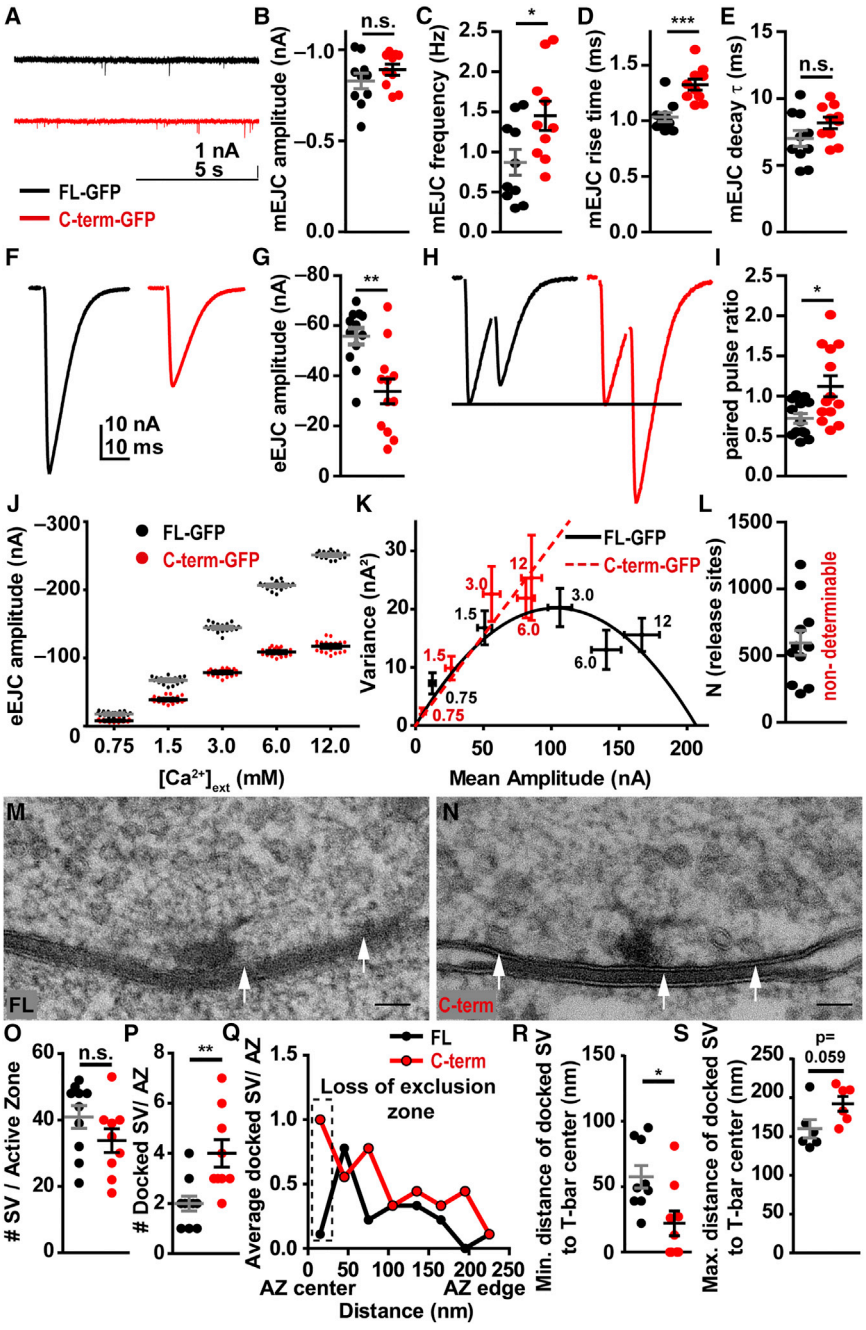

Figure 5. The Unc13A C-Terminal Fragment Generates Excessive Release Sites of Low Release Probability and Unspecific Localization

Analysis of synaptic transmission and AZ ultrastructure in *unc13*^{null} larvae rescued with either full-length Unc13A-GFP (FL-GFP, black) or the C-term-GFP fragment (red).

(A) Representative mEJC traces.

(B–E) Quantification of mEJC amplitudes (B), frequencies (C), rise times (D; 10% to 90%), and decay times (E).

(F and G) Representative eEJC (F) and quantification (G).

(H) Normalized representative paired-pulse eEJC traces with 10 ms ISI.

(I) Quantification of paired-pulse ratios. Recordings in (A)–(I) were performed in the presence of 1.5 mM $[Ca^{2+}]_{ext}$.

(J) Scatterplot of eEJC amplitudes at indicated $[Ca^{2+}]_{ext}$ from representative single cells expressing FL-GFP or C-term-GFP.

(K) Variance-mean relationship in both genotypes. Average mean amplitudes and average variances at the indicated $[Ca^{2+}]_{ext}$ are shown. Line and dashed line represent best fit models to the full dataset of either genotype. Variances continuously increased in cells expressing the C-term-GFP.

(L) In the FL-GFP condition, N could be determined in each cell by fitting the variance-mean relationship with a parabola. Due to non-parabolic behavior in C-term-GFP-expressing cells, N could not be determined.

(M and N) HPF-EM micrographs of AZ from unc13null animals rescued with either full-length Unc13A (M) or the C-term Unc13A fragment (N). Docked SVs are indicated with white arrows.

(O and P) Number of total (O) and docked (P) SVs per AZ.

(Q) Average number of docked SVs within certain bins of distances from the T-bar center.

(R and S) Minimal (R; Min.) and maximal (S; Max.) distance of docked SVs to the T-bar pedestal center per AZ. Figure source data, number of experiments and p values: see Table S1.

Scale bar in (M) and (N), 50 nm. Statistics: t test for (B)–(E), (G), (I), and (L) and Mann-Whitney U test for (O), (P), (R), and (S). *p ≤ 0.05; **p ≤ 0.01; ***p ≤ 0.001; ns, not significant, p > 0.05. All panels show mean ± SEM. For further details, see Figures S5 and S6.

scaffold, which we investigated further. Both our variance-mean experiments and ultrastructural analysis suggested more release sites upon expression of the C-terminal fragment, most of which, however, did not contribute to transmission induced by single APs. We wondered to what degree this would change upon repetitive stimulation where distant sites may be recruited by a buildup of presynaptic Ca^{2+} (Neher, 2015). To investigate this, we probed synaptic transmission in response to 60-Hz AP trains (in the presence of 2.5 mM extracellular Ca^{2+}) at NMJs of *unc13*^{null} animals expressing the C-term-GFP fragment or FL-GFP (Figure 6A). While initial responses were reduced in motoneurons expressing the C-term-GFP fragment, repetitive stimulation increased eEJCs, which happened to be similar to control responses by the 20th AP in this stimulation paradigm (Figures 6A and 6B). This was caused by a strong facilitation of responses (Figures 6C and 6D), beginning with the second stimulus already which mainly increased asynchronous release components (Figures S7A and S7B). Furthermore, synaptic transmission via the C-term-GFP fragment suffered from increasingly delayed time-to-peak values (time between the stimulation to the peak current)

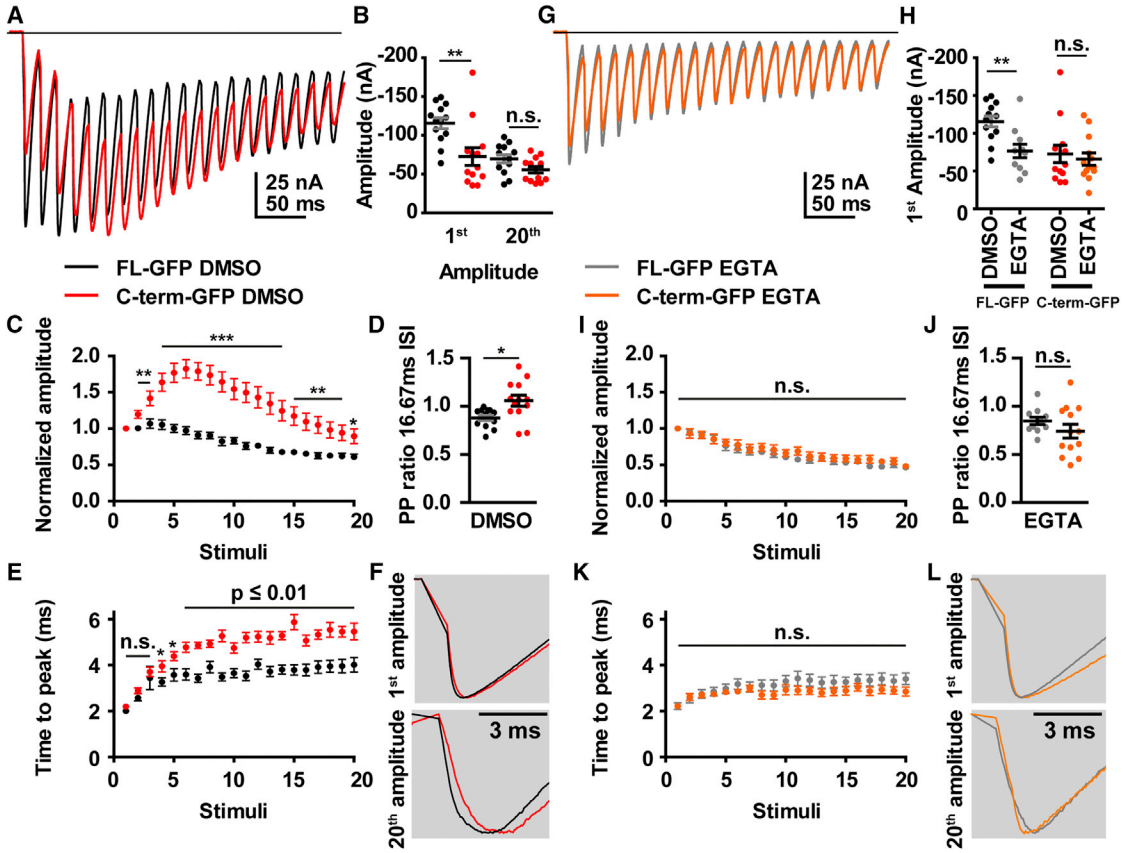

Figure 6. Synaptic Transmission Operating via the C-Terminal Fragment Shows Prominent Facilitation and Delayed and Asynchronous Release, which Is Restored by EGTA Treatment

(A) Average eEJC traces of *unc13*^{null} larvae expressing either FL-GFP (control, black) or C-term-GFP (red) in response to 60-Hz trains. Responses to the first 20 APs are shown in the absence of EGTA (but in the presence of the vehicle DMSO) for either genotype (full train shown in Figure S6).

(B) Quantification of eEJC amplitudes in response to the first and the 20th stimulation.

(C) eEJC amplitudes of the train normalized to the first amplitude and plotted against stimuli number.

(D) The 16.67 ms ISI paired-pulse ratio for the first two stimuli (synchronous component).

(E) Time-to-peak values per stimulus plotted against stimulus number.

(F) Average, normalized eEJC amplitudes of the first and the 20th stimulus.

(G) Same experiment as in (A) but in the presence of EGTA (full train in Figure S6).

(H) Genotype-specific quantification of the first eEJC amplitude in a 60-Hz train in the presence of DMSO or EGTA.

(I–L) Same analysis as in (C)–(F) in the presence of EGTA.

Figure source data, number of experiments and p values: see Table S1. Statistics: Mann-Whitney U test except for (C), (E), (I), and (K) where a t test was used. *p ≤ 0.05; **p ≤ 0.01; ***p ≤ 0.001; ns, not significant, p > 0.05. All panels show mean ± SEM. The bath solution contained 2.5 mM Ca^{2+}. For further details, see Figures S7 and S8.

during the train (Figures 6E and 6F). Both effects became even stronger at higher stimulation frequencies of 100 Hz (Figures S8A and S8B), demonstrating a requirement on the Unc13A N terminus to maintain synchronous transmission during repetitive stimulation. Analysis of linear fits to the cumulative synchronous release revealed strongly reduced slopes in the C-term-GFP-expressing animals, suggesting a slower forward priming rate (Figures S8C–S8E), which may relate to a defect in release site replenishment (Neher, 2015).

Because the expression of the C-terminal fragment resulted in additional SV docking at positions closer and further away from the AZ center, we speculated about an involvement of release sites with shorter and longer coupling distances to Ca^{2+} channels in this genotype. Especially the successive activation of more distant sites in the course of the AP train may explain the loss of temporal precision in transmission. To investigate this, we performed experiments in the presence of the exogenous Ca^{2+} buffer EGTA, which competes with the SV release machinery for Ca^{2+} and therefore differentially inhibits release based on the release site/Ca^{2+} channel distance: distant sites require longer Ca^{2+} diffusion times, increasing the chance for the buffer to bind Ca^{2+} (thereby decreasing the chances of Ca^{2+} activating the SV fusion machinery; Eggermann et al., 2011). To study the effects of EGTA in both genotypes, larvae were incubated in 100 μM of EGTA-AM (an esterified, membrane permeable version) for 30 min before recordings. Following EGTA loading,

synaptic transmission upon 60 Hz stimulation was less asynchronous in both genotypes (Figure 6G; Figures S7C and S7D). In control cells, EGTA significantly reduced eEJCs evoked by the first AP stimulus, indicative of relatively loose coupling between SV release sites and Ca^{2+} channels (Figure 6H) (Böhme et al., 2016). Strikingly, no significant effect of EGTA on the first eEJCs was observed in cells expressing the C-term-GFP fragment (Figure 6H), suggesting an involvement of release sites with even shorter coupling distances than in control cells, in agreement with the loss of an exclusion zone (Figures 5Q and 5R). However, upon repetitive stimulation, EGTA primarily inhibited asynchronous synaptic activity in these cells, blocking the unusually strong facilitation in this genotype (Figures 6G–6L; Figures S7A–S7D). In fact, EGTA treatment led to largely similar short-term plasticity features as in control synapses (Figures 6I and 6J). Moreover, EGTA also restored the timing of neurotransmission by synchronizing release during the AP train (Figures 6K and 6L). Thus, blocking the activation of distant release sites with EGTA restores short-term plasticity and temporal coding in synapses expressing the C-term-GFP fragment, indicating that the Unc13A N terminus functions in restrictive release site positioning with respect to Ca^{2+} channels.

DISCUSSION

At the synapse, transmitter release is restricted to a fixed number of highly specialized release sites where SV fusion occurs in an all or none fashion, resulting in binomial statistics of synaptic transmission (McLachlan, 1978; Vere-Jones, 1966). This feature has been used to establish release site numbers in various animal model systems, demonstrating how fundamental release site directed SV fusion is to synaptic transmission (Miki et al., 2016; Müller et al., 2012; Scheuss and Neher, 2001; Zucker, 1973). Proper release site placement with respect to presynaptic voltage-gated Ca^{2+} channels is of central importance for SV-fusion efficacy (Keller et al., 2015; Meinrenken et al., 2002; Nakamura et al., 2015; Wadel et al., 2007). AZ scaffolding proteins are not only important for Ca^{2+} channel clustering, but also for SV docking and the regulation of the number of AZ release sites (Acuna et al., 2015, 2016; Han et al., 2011; Kaeser et al., 2011; Kittel et al., 2006; Matkovic et al., 2013; Wang et al., 2016), suggesting a function in the precise coupling of release sites to the Ca^{2+} channels. However, the exact molecular "milieu" generating release sites at the AZ had not been properly understood. Here, we identify Unc13A as a release site generating molecule and show the functional relevance of proper release site localization at the AZ for synaptic function.

The local amounts of AZ scaffolding proteins predict their probability to engage in AP-evoked release (Muhammad et al., 2015; Peled et al., 2014; Tang et al., 2016). However, in our experiments this positive relation on BRP was weakened upon Unc13A-knockdown (Figures 2E and 2F), suggesting that AZ scaffolds couple to the functional AZ status via (M)Unc13 recruitment. Accordingly, AZ scaffold disruptions in several model organisms (BRP/RBP in *Drosophila* and RIM/RBP or RIM/ELKS in mouse) resulted in severe reductions of (M)Unc13 and were all paralleled by dramatically decreased synaptic transmission (Acuna et al., 2016; Böhme et al., 2016; Wang et al., 2016).

What is the molecular basis of (M)Unc13 AZ recruitment? At mammalian and *C. elegans* AZs, (M)Unc13 localization depends on an N-terminal C2A domain (which binds RIM) (Deng et al., 2011; Hu et al., 2013; Zhou et al., 2013). Although this motif is lacking in *Drosophila* Unc13A, we show that its N-terminal domains (which bind BRP and RBP; Böhme et al., 2016) also function in AZ targeting: their loss resulted in AZ-unspecific distribution of the remaining protein (Figures 3E, 3F, 3J, and 3K; Figures S3J and S3K), and an N-terminal fragment was sufficient for specific and highly stable AZ localization (Figures 3E, 3F, 3H, 3J, and 3K; Figures S3A–S3F). A similar mechanism of bMunc13-2 recruitment via its N terminus to the mammalian BRP homolog ELKS was recently described (Kawabe et al., 2017). We show that unspecific localization of the C-terminal Unc13A fragment generated docking and release sites in atypical locations, while the overexpression of the N-terminal fragment in wild-type flies displaced endogenous Unc13A (Figure S4; Figure 7B) and decreased the number of functional release sites (Figure 4). The fact that manipulations of Unc13 levels, localization, and stability were causally related to changes of release site numbers, position, and function imply a direct involvement of Unc13A in release site generation. Consistent with this being a general function of (M)Unc13 proteins, their deletion in nematodes, *Drosophila*, and mammals results in a complete halt of synaptic transmission (Aravamudan et al., 1999; Richmond et al., 1999; Varoqueaux et al., 2002).

We investigated whether spontaneous synaptic transmission at single AZs was related to local BRP/Unc13A levels and discovered a positive correlation in both cases (Figures 2E and 2F; Figures S2C and S2D). Previous investigation of *Drosophila rab3*^{null} mutants (in slightly different experimental conditions, see STAR Methods) revealed a negative correlation of spontaneous activity on local BRP levels (Peled et al., 2014). These genotype-specific differences may relate to Rab3's function to simultaneously recruit SVs to Unc13 at AZs by the formation of a tripartite Rab3/Unc13/RIM complex (Rizo and Xu, 2015). Additionally, the prominent re-distribution of the AZ scaffold inherent to the *rab3*^{null} genotype may favor the contribution of spontaneously active release sites generated by Unc13B at interstitial AZ positions, which contribute little to AP-evoked activity (Böhme et al., 2016). Regardless, the mechanism of altered scaffold dependence for transmission modes in the *rab3*^{null} mutant, our data clearly argue that, in the wild-type situation, both spontaneous and evoked activity modes primarily operate via release sites generated by Unc13A: first of all single AZ activities of both modes were highly correlated to local Unc13A levels (Figure 1K; Figure S2C) and second both transmission modes were similarly inhibited by the overexpression of the N-terminal fragment (Figure 4).

Restrictive Unc13 Positioning and Activation by the AZ Scaffold Mediates Efficient Synaptic Transmission

At AZs of *C. elegans,* the long and short isoforms Unc13L and Unc13S contribute to neurotransmitter release, but only Unc13L has an AZ-specific localization (Hu et al., 2013; Zhou et al., 2013). Our C-terminal fragment, which is qualitatively similar to the *C. elegans* Unc13S isoform (except for a short N-terminal domain in Unc13S), showed similar AZ-unspecific localization (Hu et al., 2013; Zhou et al., 2013) and was unstable

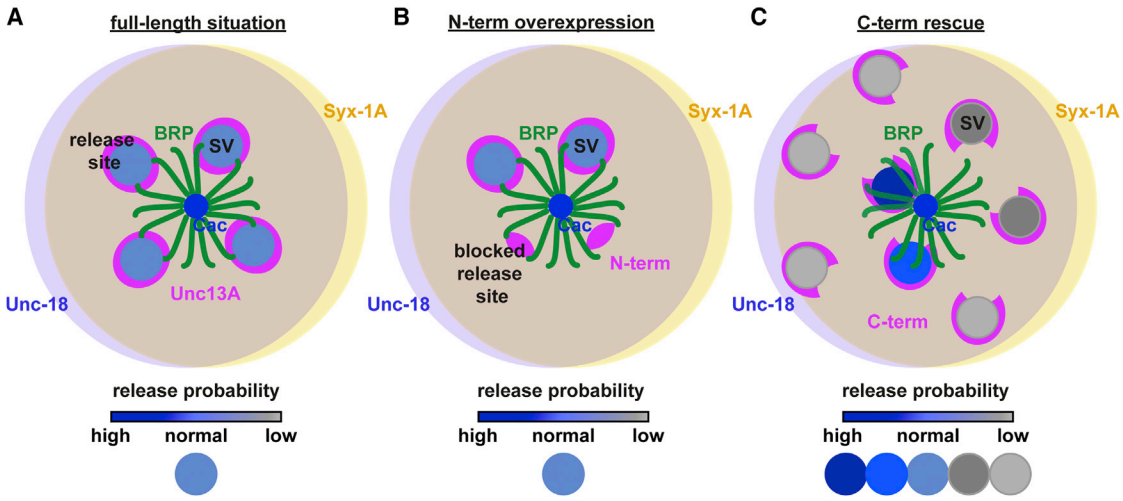

Figure 7. Release Site Situations Investigated

Schematics of BRP (green), Unc13A (magenta), Unc18 (light purple circle), Syx-1A (light yellow circle), SVs (blue circles, shading indicates different release probabilities) and the calcium channel cluster (Cac) in the AZ center (blue). Unc18 and Syx-1A are broadly distributed in the Unc13A FL situation.

(A) BRP positions Unc13A at the AZ, restricting its localization to place release sites in well-defined proximity to the Ca^{2+} channel cluster, resulting in "normal" SV release probability (light blue).

(B) The overexpressed N-terminal fragment competes with endogenous Unc13A for the restricted AZ-scaffold interaction surfaces, blocking access for the endogenous Unc13A, and reducing the number of functional release sites (which require the Unc13A C terminus). The remaining sites operate with normal release probability (normal, light blue).

(C) Rescue with an Unc13A fragment lacking the N-terminal AZ-localization sequence (the C-terminal fragment) leads to less specific SV release site positioning, creating many more release sites than usual with a broad distribution of release probabilities, which can be higher or lower than usual (dark blue to light gray).

(Figure 3). In *Drosophila unc13*^{null} larvae rescued with the C-terminal fragment, the AZ-unspecific localization was paralleled by the excessive generation of release sites with an overall low release probability. The number of docked SVs increased and their distribution shifted dramatically. While docked SV distance distributions normally peak around 50–60 nm from the AZ center and show clear evidence of an SV exclusion zone for shorter distances at control AZs (Figures 4Q and 5Q), docking was unspecific and the exclusion zone lost in animals rescued with the C-terminal fragment (Figure 5Q). An SV docking exclusion zone was recently proposed for AZs of the murine Calyx of Held (Keller et al., 2015), suggesting an evolutionarily conserved principle. We here show that the boundaries of this exclusion zone are defined by precise Unc13A localization.

An interesting aspect of our data is that while the C-terminal fragment formed release sites in ectopic positions in an AZ-scaffold-independent manner, the endogenous, full-length protein displaced by overexpression of the N-terminal fragment could not (Figures 4 and 5). This likely relates to an Unc13A auto-inhibition via its N terminus, suggesting an intramolecular interaction between the N- and C-terminal parts of the protein that shields functional (C1, C2B, MUN) domains (Basu et al., 2005, 2007; Shin et al., 2010). Inhibition may also be caused by an N-terminal interaction of two Unc13 molecules, forming an inactive homodimer, as is the case for mammalian ubMunc13-2 (Deng et al., 2011). In mammals, this auto-inhibition is relieved by interactions of the ubMunc13-2 N terminus with RIM, but deletion of the N terminus bypasses the RIM requirement for SV priming (Deng et al., 2011). Together with our data, this suggests an evolutionarily conserved principle where (M)Unc13 proteins combine a release site generating C terminus with an auto-inhibitory N terminus, which interacts with AZ scaffolding proteins for protein localization and activation. This arrangement is uniquely suited to generate release sites with well-defined coupling distances to Ca^{2+} channels while preventing their formation elsewhere. We here show the detrimental effect of bypassing this spatial confinement in rescue experiments with the Unc13 C-terminal fragment where synaptic transmission suffered from low release probability, strong facilitation, and asynchronous and delayed release (Figures 5 and 6). We therefore suggest a hierarchy of interactions in release site formation with AZ scaffolds converging on both stable Ca^{2+} channel and (M)Unc13 positioning to generate release sites of well-defined functionality.

Apart from its mislocalization, the higher motility of the C-terminal fragment may also affect synaptic transmission. This could cause lower release site occupancy, which may contribute to the observed Poisson-like behavior (Figure 5K) (Vere-Jones, 1966). Likewise, shorter residence may impair molecular priming and cause reduced release probability, e.g., due to the formation of fewer SNARE complexes or to their impaired interactions with synaptotagmin or complexin, resulting in increased energy barriers for fusion (Mohrmann et al., 2010; Schotten et al., 2015; Zhou et al., 2015). Indeed, changes in the mEJC rise time—as seen in this genotype (Figure 5D)—were linked to changed release probability due to alterations in the number of SNAREs driving fusion (Acuna et al., 2014). Altered accessibility of the lipid binding Unc13 C1 and C2B domains may also contribute to changes in release probability (Basu et al., 2007; Shin et al., 2010). However, we could show that the observed effects were not due to the lack of the CaM domain in the C-terminal fragment, which was also

shown to regulate short-term plasticity and SV replenishment (Figure S5) (Junge et al., 2004; Lipstein et al., 2013).

While we identify an essential role of Unc13 in release site generation and localization, our results do not rule out that additional factors like scaffolding proteins or Unc18/Syx-1A serve essential roles in release site function. In fact, it seems likely that release site generation would depend on the presence of several factors (Figure 7). Indeed, our analysis of single AZ activity supports this as we see very strong dependence on local Syx-1A levels (Figures 1K and 1L). The weaker relation on Unc18 levels (Figures 1K and 1L) does not rule out an essential role in release site function but may reflect already sufficient levels at all AZs to mediate a range of activities. Nevertheless, Unc13A appears to be the limiting factor among other, highly diffusible and thus easily recruitable SV release site components, implicating Unc13A as a "gatekeeper" of synaptic transmission to exclusively dock and prime SVs only at these sites (Figure 7).

Unc13 Isoforms: An Evolutionary Perspective

Accumulating evidence in most if not all model organisms suggests the synaptic presence of at least one homolog of the long AZ-specific (M)Unc13 isoform (Munc13-1/ubMunc13-2/Unc13A/Unc13L). These homologs are likely to exhibit similar functions at synapses that follow an evolutionarily conserved design optimized for speed and reliable transmission. Specializations of synapse types and functionalities might relate to different synaptic localizations of (M)Unc13 proteins encoded in their N-terminal domains. For example, neurotransmitter release at the *C. elegans* NMJ depends on both the AZ-localized Unc13L and the AZ-unspecific Unc13S (Hu et al., 2013; Zhou et al., 2013). In contrast, some of the best-characterized Unc13 variants driving synaptic transmission in *Drosophila* (Unc13A and -B) and murine synapses (Munc13-1, ubMunc13-2, bMunc13-2) all appear to localize specifically (Andrews-Zwilling et al., 2006; Böhme et al., 2016; Grauel et al., 2016; Kawabe et al., 2017). This adaptation of particular localization could give some insights into how systems are optimized to different activating stimuli. For instance, it may be an advantage to distribute SVs over larger distances from the Ca^{2+} source at the *C. elegans* NMJ to allow sensitive activation to graded responses (Liu et al., 2009), while we clearly show the disadvantages of such SV distributions in systems relying on AP-driven responses (especially during high-frequency stimulation, Figure 6). Accordingly, it is conceivable that the non-neuronal Munc13-4 isoform, which lacks the N-terminal sequence, preferably functions in systems relying on AP-independent activation. Thus, release site localization and/or motility might be an evolutionary mechanism to adapt to various types of activating stimuli.

STAR★METHODS

Detailed methods are provided in the online version of this paper and include the following:

- KEY RESOURCES TABLE
- CONTACT FOR REAGENT AND RESOURCE SHARING
- EXPERIMENTAL MODEL AND SUBJECT DETAILS
  - Fly Husbandry, Stocks, and Handling
- METHOD DETAILS
  - Generation of Syx-1A-GFP, Unc18-GFP, N-Term-GFP, FL, C-Term, C-Term-GFP, Unc13 $CaM^{W1620R,W1622R}$, and MHC-myrGCaMP5G
  - Generation of Unc13C-Term Antibody
  - Immunostaining
  - Image Acquisition, Processing, and Analysis
  - STED Microscopy and Analysis
  - Electron Microscopy/HPF and Morphometric Analysis
  - In Vivo Live Imaging and Analysis
  - GCaMP Imaging, Immunostainings, and Activity Quantification
  - Electrophysiology
  - Ca^{2+} Buffering with EGTA-AM (TEVC)
- QUANTIFICATION AND STATISTICAL ANALYSIS
- DATA AND SOFTWARE AVAILABILITY

SUPPLEMENTAL INFORMATION

Supplemental Information includes eight figures, one table, and one movie and can be found with this article online at http://dx.doi.org/10.1016/j.neuron.2017.08.016.

AUTHOR CONTRIBUTIONS

S.R.-A., M.A.B., S.J.S., and A.M.W. conceived the project. M.A.B., M.M.M., M.J., and U.R. performed confocal and *in vivo* imaging experiments and analyzed the data. A.T.G. and M.J. performed GCaMP experiments and analyzed the data. M.A.B. performed STED experiments and M.A.B. and A.T.G. analyzed the data. S.R.-A., E.R., C.B., M.J., and Z.M. performed electrophysiological experiments and E.R., C.B., M.J., A.W.M., and Z.M. analyzed the data. M.A.B., C.B., C.Q., D.D.B. and T.M. performed HPF experiments, and C.B., A.T.G., and M.M. analyzed the data. M.M.M., H.B., T.M., and D.O. created cDNA constructs. F.G. and S.W.H. developed and built the STED microscope. S.R.-A., M.A.B., S.J.S., and A.M.W. wrote the paper with input from all co-authors.

ACKNOWLEDGMENTS

This work was supported by grants from the Deutsche Forschungsgemeinschaft (DFG) to S.J.S. (Exc 257, TP A3 and A6 SFB958, TP B9/SFB665; TP09, TPZ1 (with T.M.) SFB740) and A.M. Walter (the Emmy Noether Programme and TRR186). M.A. Böhme was supported by DFG-funded Ph.D. fellowships (GRK 1123 and SFB 740), and A.T.G. was supported by a DFG-funded Ph.D. fellowship (NeuroCure, Exc 257) within the International Graduate Program Medical Neurosciences. U.R. was supported by a fellowship of the International Max Planck Research School (IMPRS). We are grateful to Troy J. Littleton for the donation of pBI-UASc-myrGCaMP5G. We thank Janine Lützkendorf for help with cloning and Sabine Hahn, Madeleine Brünner, and Anastasia Stawrakakis for excellent technical assistance. We furthermore thank Christian Rosenmund for helpful discussions and Berit Söhl-Kielczynski for excellent technical assistance with HPF experiments.

Received: October 20, 2016
Revised: May 10, 2017
Accepted: August 9, 2017
Published: August 31, 2017

REFERENCES

Aberle, H., Haghighi, A.P., Fetter, R.D., McCabe, B.D., Magalhães, T.R., and Goodman, C.S. (2002). wishful thinking encodes a BMP type II receptor that regulates synaptic growth in Drosophila. Neuron *33*, 545–558.

Acuna, C., Guo, Q., Burré, J., Sharma, M., Sun, J., and Südhof, T.C. (2014). Microsecond dissection of neurotransmitter release: SNARE-complex assembly dictates speed and Ca^{2+} sensitivity. Neuron *82*, 1088–1100.

Acuna, C., Liu, X., Gonzalez, A., and Südhof, T.C. (2015). RIM-BPs mediate tight coupling of action potentials to Ca(2+)-triggered neurotransmitter release. Neuron *87*, 1234–1247.

Acuna, C., Liu, X., and Südhof, T.C. (2016). How to make an active zone: unexpected universal functional redundancy between RIMs and RIM-BPs. Neuron *91*, 792–807.

Andlauer, T.F., and Sigrist, S.J. (2012). Quantitative analysis of Drosophila larval neuromuscular junction morphology. Cold Spring Harb. Protoc. *2012*, 490–493.

Andrews-Zwilling, Y.S., Kawabe, H., Reim, K., Varoqueaux, F., and Brose, N. (2006). Binding to Rab3A-interacting molecule RIM regulates the presynaptic recruitment of Munc13-1 and ubMunc13-2. J. Biol. Chem. *281*, 19720–19731.

Aravamudan, B., Fergestad, T., Davis, W.S., Rodesch, C.K., and Broadie, K. (1999). Drosophila UNC-13 is essential for synaptic transmission. Nat. Neurosci. *2*, 965–971.

Basu, J., Shen, N., Dulubova, I., Lu, J., Guan, R., Guryev, O., Grishin, N.V., Rosenmund, C., and Rizo, J. (2005). A minimal domain responsible for Munc13 activity. Nat. Struct. Mol. Biol. *12*, 1017–1018.

Basu, J., Betz, A., Brose, N., and Rosenmund, C. (2007). Munc13-1 C1 domain activation lowers the energy barrier for synaptic vesicle fusion. J. Neurosci. *27*, 1200–1210.

Böhme, M.A., Beis, C., Reddy-Alla, S., Reynolds, E., Mampell, M.M., Grasskamp, A.T., Lützkendorf, J., Bergeron, D.D., Driller, J.H., Babikir, H., et al. (2016). Active zone scaffolds differentially accumulate Unc13 isoforms to tune Ca(2+) channel-vesicle coupling. Nat. Neurosci. *19*, 1311–1320.

Clements, J.D., and Silver, R.A. (2000). Unveiling synaptic plasticity: A new graphical and analytical approach. Trends Neurosci. *23*, 105–113.

Del Castillo, J., and Katz, B. (1954). Quantal components of the end-plate potential. J. Physiol. *124*, 560–573.

Deng, L., Kaeser, P.S., Xu, W., and Südhof, T.C. (2011). RIM proteins activate vesicle priming by reversing autoinhibitory homodimerization of Munc13. Neuron *69*, 317–331.

Eggermann, E., Bucurenciu, I., Goswami, S.P., and Jonas, P. (2011). Nanodomain coupling between Ca^{2+} channels and sensors of exocytosis at fast mammalian synapses. Nat. Rev. Neurosci. *13*, 7–21.

Fouquet, W., Owald, D., Wichmann, C., Mertel, S., Depner, H., Dyba, M., Hallermann, S., Kittel, R.J., Eimer, S., and Sigrist, S.J. (2009). Maturation of active zone assembly by Drosophila Bruchpilot. J. Cell Biol. *186*, 129–145.

Füger, P., Behrends, L.B., Mertel, S., Sigrist, S.J., and Rasse, T.M. (2007). Live imaging of synapse development and measuring protein dynamics using two-color fluorescence recovery after photo-bleaching at Drosophila synapses. Nat. Protoc. *2*, 3285–3298.

Göttfert, F., Wurm, C.A., Mueller, V., Berning, S., Cordes, V.C., Honigmann, A., and Hell, S.W. (2013). Coaligned dual-channel STED nanoscopy and molecular diffusion analysis at 20 nm resolution. Biophys. J. *105*, L01–L03.

Grauel, M.K., Maglione, M., Reddy-Alla, S., Willmes, C.G., Brockmann, M.M., Trimbuch, T., Rosenmund, T., Pangalos, M., Vardar, G., Stumpf, A., et al. (2016). RIM-binding protein 2 regulates release probability by fine-tuning calcium channel localization at murine hippocampal synapses. Proc. Natl. Acad. Sci. USA *113*, 11615–11620.

Han, Y., Kaeser, P.S., Südhof, T.C., and Schneggenburger, R. (2011). RIM determines Ca^{2}+ channel density and vesicle docking at the presynaptic active zone. Neuron *69*, 304–316.

Holderith, N., Lorincz, A., Katona, G., Rózsa, B., Kulik, A., Watanabe, M., and Nusser, Z. (2012). Release probability of hippocampal glutamatergic terminals scales with the size of the active zone. Nat. Neurosci. *15*, 988–997.

Hu, Z., Tong, X.J., and Kaplan, J.M. (2013). UNC-13L, UNC-13S, and Tomosyn form a protein code for fast and slow neurotransmitter release in Caenorhabditis elegans. eLife *2*, e00967.

Imig, C., Min, S.W., Krinner, S., Arancillo, M., Rosenmund, C., Südhof, T.C., Rhee, J., Brose, N., and Cooper, B.H. (2014). The morphological and molecular nature of synaptic vesicle priming at presynaptic active zones. Neuron *84*, 416–431.

Jahn, R., and Fasshauer, D. (2012). Molecular machines governing exocytosis of synaptic vesicles. Nature *490*, 201–207.

Junge, H.J., Rhee, J.S., Jahn, O., Varoqueaux, F., Spiess, J., Waxham, M.N., Rosenmund, C., and Brose, N. (2004). Calmodulin and Munc13 form a Ca2+ sensor/effector complex that controls short-term synaptic plasticity. Cell *118*, 389–401.

Kaeser, P.S., Deng, L., Wang, Y., Dulubova, I., Liu, X., Rizo, J., and Südhof, T.C. (2011). RIM proteins tether Ca2+ channels to presynaptic active zones via a direct PDZ-domain interaction. Cell *144*, 282–295.

Kawabe, H., Mitkovski, M., Kaeser, P.S., Hirrlinger, J., Opazo, F., Nestvogel, D., Kalla, S., Fejtova, A., Verrier, S.E., Bungers, S.R., et al. (2017). ELKS1 localizes the synaptic vesicle priming protein bMunc13-2 to a specific subset of active zones. J. Cell Biol. *216*, 1205.

Kawasaki, F., Zou, B., Xu, X., and Ordway, R.W. (2004). Active zone localization of presynaptic calcium channels encoded by the cacophony locus of Drosophila. J. Neurosci. *24*, 282–285.

Keller, D., Babai, N., Kochubey, O., Han, Y., Markram, H., Schürmann, F., and Schneggenburger, R. (2015). An exclusion zone for Ca2+ channels around docked vesicles explains release control by multiple channels at a CNS synapse. PLoS Comput. Biol. *11*, e1004253.

Kittel, R.J., Wichmann, C., Rasse, T.M., Fouquet, W., Schmidt, M., Schmid, A., Wagh, D.A., Pawlu, C., Kellner, R.R., Willig, K.I., et al. (2006). Bruchpilot promotes active zone assembly, Ca2+ channel clustering, and vesicle release. Science *312*, 1051–1054.

Lin, D.M., and Goodman, C.S. (1994). Ectopic and increased expression of Fasciclin II alters motoneuron growth cone guidance. Neuron *13*, 507–523.

Lipstein, N., Sakaba, T., Cooper, B.H., Lin, K.H., Strenzke, N., Ashery, U., Rhee, J.S., Taschenberger, H., Neher, E., and Brose, N. (2013). Dynamic control of synaptic vesicle replenishment and short-term plasticity by Ca(2+)-calmodulin-Munc13-1 signaling. Neuron *79*, 82–96.

Liu, Q., Hollopeter, G., and Jorgensen, E.M. (2009). Graded synaptic transmission at the Caenorhabditis elegans neuromuscular junction. Proc. Natl. Acad. Sci. USA *106*, 10823–10828.

Liu, K.S., Siebert, M., Mertel, S., Knoche, E., Wegener, S., Wichmann, C., Matkovic, T., Muhammad, K., Depner, H., Mettke, C., et al. (2011). RIM-binding protein, a central part of the active zone, is essential for neurotransmitter release. Science *334*, 1565–1569.

Liu, X., Seven, A.B., Camacho, M., Esser, V., Xu, J., Trimbuch, T., Quade, B., Su, L., Ma, C., Rosenmund, C., and Rizo, J. (2016). Functional synergy between the Munc13 C-terminal C1 and C2 domains. eLife. Published online May 23, 2016. http://dx.doi.org/10.7554/eLife.13696.

Mahr, A., and Aberle, H. (2006). The expression pattern of the Drosophila vesicular glutamate transporter: A marker protein for motoneurons and glutamatergic centers in the brain. Gene Expr. Patterns *6*, 299–309.

Matkovic, T., Siebert, M., Knoche, E., Depner, H., Mertel, S., Owald, D., Schmidt, M., Thomas, U., Sickmann, A., Kamin, D., et al. (2013). The Bruchpilot cytomatrix determines the size of the readily releasable pool of synaptic vesicles. J. Cell Biol. *202*, 667–683.

McLachlan, E.M. (1978). The statistics of transmitter release at chemical synapses. Int. Rev. Physiol. *17*, 49–117.

Meinrenken, C.J., Borst, J.G., and Sakmann, B. (2002). Calcium secretion coupling at calyx of Held governed by nonuniform channel-vesicle topography. J. Neurosci. *22*, 1648–1667.

Melom, J.E., Akbergenova, Y., Gavornik, J.P., and Littleton, J.T. (2013). Spontaneous and evoked release are independently regulated at individual active zones. J. Neurosci. *33*, 17253–17263.

Miki, T., Malagon, G., Pulido, C., Llano, I., Neher, E., and Marty, A. (2016). Actin- and myosin-dependent vesicle loading of presynaptic docking sites prior to exocytosis. Neuron *91*, 808–823.

Mohrmann, R., de Wit, H., Verhage, M., Neher, E., and Sørensen, J.B. (2010). Fast vesicle fusion in living cells requires at least three SNARE complexes. Science *330*, 502–505.

Muhammad, K., Reddy-Alla, S., Driller, J.H., Schreiner, D., Rey, U., Böhme, M.A., Hollmann, C., Ramesh, N., Depner, H., Lützkendorf, J., et al. (2015). Presynaptic spinophilin tunes neurexin signalling to control active zone architecture and function. Nat. Commun. *6*, 8362.

Müller, M., Liu, K.S., Sigrist, S.J., and Davis, G.W. (2012). RIM controls homeostatic plasticity through modulation of the readily-releasable vesicle pool. J. Neurosci. *32*, 16574–16585.

Nakamura, Y., Harada, H., Kamasawa, N., Matsui, K., Rothman, J.S., Shigemoto, R., Silver, R.A., DiGregorio, D.A., and Takahashi, T. (2015). Nanoscale distribution of presynaptic Ca(2+) channels and its impact on vesicular release during development. Neuron *85*, 145–158.

Neher, E. (2010). What is rate-limiting during sustained synaptic activity: vesicle supply or the availability of release sites. Front. Synaptic Neurosci. *2*, 144.

Neher, E. (2015). Merits and limitations of vesicle pool models in view of heterogeneous populations of synaptic vesicles. Neuron *87*, 1131–1142.

Newman, Z.L., Hoagland, A., Aghi, K., Worden, K., Levy, S.L., Son, J.H., Lee, L.P., and Isacoff, E.Y. (2017). Input-specific plasticity and homeostasis at the Drosophila larval neuromuscular junction. Neuron *93*, 1388–1404.

Peled, E.S., Newman, Z.L., and Isacoff, E.Y. (2014). Evoked and spontaneous transmission favored by distinct sets of synapses. Curr. Biol. *24*, 484–493.

Pertsinidis, A., Mukherjee, K., Sharma, M., Pang, Z.P., Park, S.R., Zhang, Y., Brunger, A.T., Südhof, T.C., and Chu, S. (2013). Ultrahigh-resolution imaging reveals formation of neuronal SNARE/Munc18 complexes in situ. Proc. Natl. Acad. Sci. USA *110*, E2812–E2820.

Qin, G., Schwarz, T., Kittel, R.J., Schmid, A., Rasse, T.M., Kappei, D., Ponimaskin, E., Heckmann, M., and Sigrist, S.J. (2005). Four different subunits are essential for expressing the synaptic glutamate receptor at neuromuscular junctions of Drosophila. J. Neurosci. *25*, 3209–3218.

Richmond, J.E., Davis, W.S., and Jorgensen, E.M. (1999). UNC-13 is required for synaptic vesicle fusion in C. elegans. Nat. Neurosci. *2*, 959–964.

Rizo, J., and Xu, J. (2015). The synaptic vesicle release machinery. Annu. Rev. Biophys. *44*, 339–367.

Scheuss, V., and Neher, E. (2001). Estimating synaptic parameters from mean, variance, and covariance in trains of synaptic responses. Biophys. J. *81*, 1970–1989.

Schotten, S., Meijer, M., Walter, A.M., Huson, V., Mamer, L., Kalogreades, L., ter Veer, M., Ruiter, M., Brose, N., Rosenmund, C., et al. (2015). Additive effects on the energy barrier for synaptic vesicle fusion cause supralinear effects on the vesicle fusion rate. eLife *4*, e05531.

Schulze, K.L., Littleton, J.T., Salzberg, A., Halachmi, N., Stern, M., Lev, Z., and Bellen, H.J. (1994). rop, a Drosophila homolog of yeast Sec1 and vertebrate n-Sec1/Munc-18 proteins, is a negative regulator of neurotransmitter release in vivo. Neuron *13*, 1099–1108.

Schulze, K.L., Broadie, K., Perin, M.S., and Bellen, H.J. (1995). Genetic and electrophysiological studies of Drosophila Syntaxin-1A demonstrate its role in nonneuronal secretion and neurotransmission. Cell *80*, 311–320.

Shin, O.H., Lu, J., Rhee, J.S., Tomchick, D.R., Pang, Z.P., Wojcik, S.M., Camacho-Perez, M., Brose, N., Machius, M., Rizo, J., et al. (2010). Munc13 C2B domain is an activity-dependent Ca2+ regulator of synaptic exocytosis. Nat. Struct. Mol. Biol. *17*, 280–288.

Sigrist, S.J., Reiff, D.F., Thiel, P.R., Steinert, J.R., and Schuster, C.M. (2003). Experience-dependent strengthening of Drosophila neuromuscular junctions. J. Neurosci. *23*, 6546–6556.

Stewart, B.A., Atwood, H.L., Renger, J.J., Wang, J., and Wu, C.F. (1994). Improved stability of Drosophila larval neuromuscular preparations in haemolymph-like physiological solutions. J. Comp. Physiol. A Neuroethol. Sens. Neural Behav. Physiol. *175*, 179–191.

Südhof, T.C. (2012). The presynaptic active zone. Neuron *75*, 11–25.

Tang, A.H., Chen, H., Li, T.P., Metzbower, S.R., MacGillavry, H.D., and Blanpied, T.A. (2016). A trans-synaptic nanocolumn aligns neurotransmitter release to receptors. Nature *536*, 210–214.

Ullrich, A., Böhme, M.A., Schöneberg, J., Depner, H., Sigrist, S.J., and Noé, F. (2015). Dynamical organization of Syntaxin-1A at the presynaptic active zone. PLoS Comput. Biol. *11*, e1004407.

Varoqueaux, F., Sigler, A., Rhee, J.S., Brose, N., Enk, C., Reim, K., and Rosenmund, C. (2002). Total arrest of spontaneous and evoked synaptic transmission but normal synaptogenesis in the absence of Munc13-mediated vesicle priming. Proc. Natl. Acad. Sci. USA *99*, 9037–9042.

Vere-Jones, D. (1966). Simple stochastic models for the release of quanta of transmitter from a nerve terminal. Aust. J. Stat. *8*, 53–63.

Wadel, K., Neher, E., and Sakaba, T. (2007). The coupling between synaptic vesicles and Ca2+ channels determines fast neurotransmitter release. Neuron *53*, 563–575.

Wang, S.S., Held, R.G., Wong, M.Y., Liu, C., Karakhanyan, A., and Kaeser, P.S. (2016). Fusion competent synaptic vesicles persist upon active zone disruption and loss of vesicle docking. Neuron *91*, 777–791.

Wilhelm, B.G., Mandad, S., Truckenbrodt, S., Kröhnert, K., Schäfer, C., Rammner, B., Koo, S.J., Claßen, G.A., Krauss, M., Haucke, V., et al. (2014). Composition of isolated synaptic boutons reveals the amounts of vesicle trafficking proteins. Science *344*, 1023–1028.

Zhou, K., Stawicki, T.M., Goncharov, A., and Jin, Y. (2013). Position of UNC-13 in the active zone regulates synaptic vesicle release probability and release kinetics. eLife *2*, e01180.

Zhou, Q., Lai, Y., Bacaj, T., Zhao, M., Lyubimov, A.Y., Uervirojnangkoorn, M., Zeldin, O.B., Brewster, A.S., Sauter, N.K., Cohen, A.E., et al. (2015). Architecture of the synaptotagmin-SNARE machinery for neuronal exocytosis. Nature *525*, 62–67.

Zucker, R.S. (1973). Changes in the statistics of transmitter release during facilitation. J. Physiol. *229*, 787–810.

STAR★METHODS

KEY RESOURCES TABLE

REAGENT or RESOURCE	SOURCE	IDENTIFIER
Antibodies		
Guinea-pig Unc13A	Böhme et al., 2016	N/A
Mouse monoclonal Syx-1A 8C3	Developmental Studies Hybridoma Bank	Cat# 8c3, RRID: AB_528484
Mouse Rop 4F8	Developmental Studies Hybridoma Bank	Cat# Rop 4F8, RRID: AB_1157869
Rabbit Unc13-C-term	This paper	N/A
Mouse monoclonal GFP 3E6	Thermo Fisher Scientific	Cat# A-11120, RRID: AB_221568
Rabbit GFP	Thermo Fisher Scientific	Cat# A-11122, RRID: AB_221569
Mouse monoclonal NC82	Developmental Studies Hybridoma Bank	Cat# nc82, RRID: AB_2314865
Rabbit $BRP^{Last200}$	Ullrich et al., 2015	N/A
Goat anti-HRP-Cy5	Jackson ImmunoResearch	N/A
Goat anti-rabbit-Cy3	Jackson ImmunoResearch	Cat# 111-165-144, RRID: AB_2338006
Goat anti-mouse-Cy3	Jackson ImmunoResearch	Cat# 115-165-146, RRID: AB_2338690
Goat ant-rabbit-Cy5	Jackson ImmunoResearch	Cat# 111-175-144, RRID: AB_2338013
Donkey anti guinea-pig DyLight 405	Jackson ImmunoResearch	Cat# 106-475-003, RRID: AB_2337432
Goat anti-mouse Alexa 488	Life Technologies	Cat# A11001, RRID: AB_2534069
Goat anti guinea-pig Alexa 488	Life Technologies	Cat# A11073, RRID: AB_2534117
Goat anti-mouse Atto590	This paper; ATTO-TEC; Dianova	Atto590: Cat#AD 590-31
Goat anti-rabbit Atto590	This paper; ATTO-TEC; Dianova	Atto590: Cat#AD 590-31
Goat anti-guinea pig star635	This paper; Abberior; Dianova	Star635: Cat#1-0101002-1
Goat anti-rabbit star635	This paper; Abberior; Dianova	Star635: Cat#1-0101002-1
Critical Commercial Assays		
pENTR/D-TOPO Cloning Kit	Thermo Fisher Scientific	Cat. No. K240020
Gateway reaction kit BP clonase	Invitrogen	Cat. No. 11789-020
Gateway reaction kit LR clonase	Invitrogen	Cat. No. 11791-020
Counter-Selection BAC Modification Kit	Gene Bridges	Cat# K002
Elongase Enzyme Mix	Invitrogen	Cat. No. 10480028
Experimental Models: Organisms/Strains		
y[1] w[1118]; PBac{y[+]-attP-9A}VK00005	BestGene, CA, USA	FlyBase: FBst0009725
y[1] M{vas-int.Dm}vZH-2A w[*]; PBac{y[+]-attP-9A}VK00005	Rainbow Transgenic Flies	FlyBase: FBst0024862
y[1] w[1118]; PBac{y[+]-attP-9A}VK00027	BestGene, CA, USA	FlyBase: FBst0009744
D. melanogaster: Wild type: *w1118*	Lab stock	N/A
D. melanogaster: *Ok6-GAL4/II*	Aberle et al., 2002	N/A
D. melanogaster: *UAS-Syx-1A-GFP/III*	This paper	N/A
D. melanogaster: *UAS-Unc18-GFP/III*	This paper	N/A
D. melanogaster: *UAS-Unc13A-GFP/Tm6b*	Böhme et al., 2016	N/A
D. melanogaster: *Elav-Gal4/I*	Lin and Goodman, 1994	
D. melanogaster: *UAS-N-term-GFP/III*	This paper	N/A
D. melanogaster: *UAS-C-term-GFP/III*	This paper	N/A
D. melanogaster: *Ok371-GAL4/II*	Mahr and Aberle, 2006	N/A
D. melanogaster: *UAS-Unc13A/Tm6b*	This paper	N/A
D. melanogaster: *UAS-C-term/III*	This paper	N/A

(*Continued on next page*)

Continued

REAGENT or RESOURCE	SOURCE	IDENTIFIER
D. melanogaster: *CaM^{W1620R,W1622R}/III*	This paper	N/A
D. melanogaster: *Unc13B^{null}*/III	Böhme et al., 2016	N/A
D. melanogaster: UAS-Unc13A-RNAi/III	This paper	N/A
D. melanogaster: *Mhc-myr-gcamp5g/III*	This paper	N/A
D. melanogaster: *Unc13^{null}: ry506 ; P{ry11}unc-13P84200 / ciD*	Kyoto Stock Center	FlyBase: FBst0300878
E.coli competent cells DH5α	Invitrogen	Cat# 18265-017
Oligonucleotides		
Primer: Unc13-IsoA-Nterm-FW 5′- CACCA TGACGCACTACGTGAGGC-3′	This paper	N/A
Primer: Unc13-IsoA-Nterm-Rev 5′- ATTAA GCTGCATGATTATTTTATTG-3′	This paper	N/A
Primer: Unc13-Cterm-FW 5′- CACCATGC ATCCCGGTGACAATCCATTC-3′	This paper	N/A
Primer: Unc13-Cterm-Rev 5′-TGTACCCA TGGTTGGCTCCT-3′	This paper	N/A
Primer: Unc13-1859 FW 5′-CACCATGCG CACTACGTGAGGC-3′	This paper	N/A
Primer: Unc13-1859 REV 5′-AGGCTTCA GATACTCAGATATG-3′	This paper	N/A
Primer: Syntaxin_for 5-CACCATGACTA AAGACAGATTAGCC-3′	This paper	N/A
Primer: Syntaxin_rev 5′-CATGAAATAAC TGCTAACATATG-3′	This paper	N/A
Primer: 0805DO-rop-fw 5′-GTCTATACTA GTATGGCCTTGAAAGTGCT-3′	This paper	N/A
Primer: 0805DO-rop-rev 5′-GTCTATGGTA CCGTCCTCCTTCGAGAGAGAACT-3′	This paper	N/A
Primer: CaM mutation fw primer: 5′-CAGC TCGGCAACGACGGCATCGGGC-3′	This paper	N/A
Primer: CaM mutation rv primer: 5′-GCCC GATGCCGTCGTTGCCGAGCTG-3′	This paper	N/A
Primer: HB-UB2 FW 5′-CAGAATTCTACC CAGCATGGTTCGAG-3′	This paper	N/A
Primer: HB-UB2 REV 5′-TAGCGGCCGCT CAGTTCCTTTGAGCTGCA-3′	This paper	N/A
Primer: UNC13A-RNAi-fw 5′-CTAGCAGT GGGTTAGGACATAATAATCTATAGTTAT ATTCAAGCATATAGATTATTATGTCCTA ACCCGCG-3′	This paper	N/A
Primer: Unc13A-RNAi-rev 5′- AATTCGC GGGTTAGGACATAATAATCTATATGCT TGAATATAACTATAGATTATTATGTCCT AACCCACTG-3′	This paper	N/A
Recombinant DNA		
Gal4/UAS-vector with/without C-terminal GFP tag	Lab stock	N/A
pPgex-6p1 (GST tagged)	Amersham plc	Cat. No. 27-4597-01
pWalium20	Harvard Medical School	https://fgr.hms.harvard.edu/files/fly/files/2ndgenprotocol.pdf
cDNA LD28927	Drosophila Genomics Resource Center	FlyBase: FBcl0177248
cDNA LD15472	Drosophila Genomics Resource Center	FlyBase: FBcl0155279

(*Continued on next page*)

Continued

REAGENT or RESOURCE	SOURCE	IDENTIFIER
cDNA SD04216	Drosophila Genomics Resource Center	FlyBase: FBcl0276791
cDNA LD43943	Drosophila Genomics Resource Center	FlyBase: FBcl0170400
Software and Algorithms		
LAS X software	Leica Microsystems	http://www.leica-microsystems.com/home/
LCS AF	Leica Microsystems	http://www.leica-microsystems.com/home/
ImageJ	NIH	Version 1.48q/1.50 g; https://imagej.nih.gov/ij/
Imspector Software	Max Planck Innovation	Version 0.10
MATLAB	MathWorks	R2010b/R2016a
Clampfit	Molecular Devices	Version 10.3
Peristaltic pump	Gilson	Gilson Minipuls 3
GraphPad Prism	GraphPad Software	Version 5.01/6.01
pClamp 10	Molecular Devices	N/A
Other		
Leica SP8 microscope	Leica Microsystems	http://www.leica-microsystems.com/home/
custom-built STED-microscope	Göttfert et al., 2013	N/A
HPF machine (HPM100)	Leica Microsystems	http://www.leica-microsystems.com/home/
AFS	Leica Microsystems	http://www.leica-microsystems.com/home/
Ultramicrotome (RMC Power Tome XL; Reichert Ultracut S)	Leica Microsystems	http://www.leica-microsystems.com/home/
Electrone microscope (Tecnai Spirit; FEI or Zeiss 900)	FEI; Zeiss	https://www.fei.com; https://www.zeiss.com/

CONTACT FOR REAGENT AND RESOURCE SHARING

Further information and requests for resources and reagents should be directed to and will be fulfilled by the Lead Contact, Alexander M. Walter (awalter@fmp-berlin.de).

EXPERIMENTAL MODEL AND SUBJECT DETAILS

Fly Husbandry, Stocks, and Handling

All experiments involving genetically modified organisms have been approved by the responsible authorities (Landesamt für Gesundheit und Soziales, Berlin), and conducted in compliance with the respective German law. Fly strains were reared under standard laboratory conditions (Sigrist et al., 2003) and raised at 25°C on semi-defined medium (Bloomington recipe). For most experiments both male and female larvae were used. For electrophysiological analysis only male larvae were used. The following genotypes were used: Wild-type: +/+ (*w1118*). FRAP experiments Figure 1: Syx-1A-GFP: *Ok6-GAL4/+;UAS-Syx-1A-GFP/+.* Unc18-GFP: *Ok6-GAL4/+;UAS-Unc18-GFP/+.* Unc13-A-GFP: *Ok6-GAL4/+;UAS-Unc13A-GFP/+.* Figure 2: Control: *Ok6-GAL4/+; Mhc-myr-gcamp5g/+.* Unc13A-KD: *Ok6-GAL4/+; Mhc-myr-gcamp5g/UAS-Unc13A-RNAi.* Figure 3: FL-GFP: *elav-GAL4/+;;UAS-Unc13A-GFP/+.* N-term-GFP: *elav-GAL4/+;;UAS-N-term-GFP/+.* C-term-GFP: *elav-GAL4/+;;UAS-C-term-GFP/+.* FRAP experiments: FL-GFP: *Ok6-GAL4/+;UAS-Unc13A-GFP/+.* N-term-GFP: *Ok6-GAL4/+;UAS-N-term-GFP/+.* C-term-GFP: *Ok6-GAL4/+;UAS-C-term-GFP/+.* Figure 4: Control: *Ok371-GAL4/+.* N-term-GFP: *Ok371-GAL4/+;UAS-N-term-GFP/+.* Figure 5: FL-GFP: *elav-GAL4/+;;UAS-Unc13A-GFP/+;P84200/P84200.* C-term-GFP: *elav-GAL4/+;;UAS-C-term-GFP/+;P84200/P84200.* Figure 5: FL: *elav-GAL4/+;;UAS-Unc13A/+;P84200/P84200.* C-term: *elav-GAL4/+;;UAS-C-term/+;P84200/P84200.* Figure 6; Figures S5–S7: FL-GFP: *elav-GAL4/+;;UAS-Unc13A-GFP/+;P84200/P84200.* C-term-GFP: *elav-GAL4/+;;UAS-C-term-GFP/+;P84200/P84200.*

FL-GFP: Ok6-GAL4/+;UAS-Unc13A-GFP/+. Figures S2A–S2F: FL-GFP: elav-GAL4/+;;UAS-Unc13A-GFP/+. N-term-GFP: elav-GAL4/+;;UAS-N-term-GFP/+. Figures S2G–S2K: FL-GFP: elav-GAL4/+;;UAS-Unc13A-GFP/+;P84200/P84200. C-term-GFP: elav-GAL4/+;;UAS-C-term-GFP/+;P84200/P84200. Figure S3: Control: elav-GAL4/+. N-term-GFP: elav-GAL4/+;;UAS-N-term-GFP/+. Figure S4: $CaM^{W1620R,W1622R}$: $CaM^{W1620R,W1622R}$/$CaM^{W1620R,W1622R}$;P84200/P84200. Control: $unc13B^{null}$/$unc13B^{null}$;P84200/P84200. Figures 1I–1L; S2: Mhc-myr-gcamp5g/+.

Stocks were obtained from: *Ok6-GAL4* (Aberle et al., 2002); *Ok371-GAL4* (Mahr and Aberle, 2006); *elav-Gal4* (Lin and Goodman, 1994); *UAS-Unc13A-GFP, unc13B*^{null} (Böhme et al., 2016). *P84200* was provided by the Kyoto stock center.

METHOD DETAILS

Generation of Syx-1A-GFP, Unc18-GFP, N-Term-GFP, FL, C-Term, C-Term-GFP, Unc13 CaM^{W1620R,W1622R}, and MHC-myrGCaMP5G

N-Term-GFP

The N-term of Unc13A (1-1632 AA) was amplified from Unc13A cDNA and cloned into pENTR/D-Topo (Invitrogen) using the following primers:

Unc13-IsoA-Nterm-FW 5′- CACCATGACGCACTACGTGAGGC −3′
Unc13-IsoA-Nterm-Rev 5′- ATTAAGCTGCATGATTATTTTATTG-3′

Giving Rise to the Following Protein Sequence (1-1632 AA)

MTHYVRHDYFHNTQNGALSSDTSRISYSQISYETQPSREYFSESYALSNQGPEECSRVSHLNSDTVLTTVDNSNNSYGYDYLECYGANI
QCDPEEDSVDNWNENTSVVADQYGLGHNNLNCTSSKLLPKLPNIENGRGSSNACAPQMDVKFNTKGMCIKIDHSYGVCMAKAHDFV
GRLSPSDYQNILGNNLNGYAGCAYSSTFLDNAMSSAPLRVLPQSPRCSSYLGRNIIGFNADAAQRDGRGFDTDQTDAMGSESSTYEVY
EKMQRPYTSMLPLDYSDYQEGCYNTDNLSTYSDTPPSNNTQLKRQMQRKISLMMAMTTASVIASGEIRVPVHSKQSKKSTEIQTDSIIG
NTISTNAAARDLDRCLATESCEVIVDTRDSGSVTSFPSSAVTAITKTRKLPKVLPTPLCKSSRHPITIATDALSSSYTSDPLPEKSHRPKQLP
KLPISLPQSNDRASLNSNWATPPAPDALPFNSFDHKSASSPTPTTTITKDTETTSYLVETDFIGARHNALYQYDSKEPNIVFSDKSVEAEH
SPTWTPLSPIQSKQSPCPPVALPSNIMQNVSLTCHLPEIEATRSDIEREPESSSIEPILEIEKLADPYSGPGSALFNISEYLKPYTLNKPILSE
EKKNHIANAASTSTTTPLNITSDDEFSSYSNKWTSTCVNFQPLDVESSLNISLKVNAGTNQAELLMTPLKSSTPLFISSNGTSDNFNLRKS
SPPDSAFTTTVNVNSFETVLVSGSQTASPSPSNLKSPPSIAPLLSYSDYMKQFELPELPQPIMDLSENDTATQSDSFNVINNTLTNADNLN
SYNQMDVESKSSLQLPSYSSESFDPCSVPSFSIKNKEYKIVEKLDSLSNVESVESPKTLVSPVNPLNCSKLLPGTESIVSNDVAFDDTFYD
SFNVDIKELTAFVDHVAPEDGLYNFPNDKTSVEFSFDKTEDTIDMNQNLSSGECGYYKPSQAQQKASVVASAASSVLDGISKGLKGGLD
GVFSGVSSTVDVTQSNPSSKRGFSFNLASKIVPSVGGLLTSTSSTSIKQTGSETNPTLILISPENVSSRNSNYIPTTSPSCTQKNGEENLYS
ATVHNKSTKSNSYYNEVGEISSTLVRNVCDSYDNSYDEMILTNEMVNIGMLDSESEFGLIENSYSYQVPDNEQIDSVNSYNNKTQNVTN
NGIEKANTKNKPVPLHDPPTKKASTVGMFGSILGKAAAAVQSATQAVNQSASSVASVVAQKPTIVPRTNNVLLLSSVCSPNEIKRNSSSV
EFDSEYGYQMPDVESLSSHYANTGGDYDNSNMKIHEFGTYADDRPYADYHTNGNQSQFKEEAVIPGEPEVINTNILPIGPQATGKKLPT
VNGKSALLIKQMPTEVYDDESDTDELDVSPSTGKVPSYSIYSEQEDYYMDLQQTTPSIQPNGFYEQVNNGYDYREDYFNEEDEYKYLEQ
QREQEEHNQPKNKKYLKQAKISKIQPPSLDFIDVGQDDDFIYDNYHSEDDSGNYLEGSSSGSVGPIEGSIIKVDSNIEASFASLNKKSDSF
TPTNDSLQKHDTVIGESTTKLTRLRTEKMCPDVDEEDENLSDHVSDLTDLSKLISQKKKTLLRGETEEVVGGHMQVLRQTEITARQRWH
WAYNKIIMQLN.

Through Gateway reaction (Invitrogen, CA, UAS), the construct was shuttled into GAL4/UAS vector with C-terminal GFP tag.

For the generation of transgenic flies the construct was sent for DNA micro-injection into embryos to BestGene Inc, CA, USA using the PhiC31 integration system. The construct was inserted at the genomic position 75A10, 3L:17952108.17952108 (r6, Ti) (9725 fly strain; service type: H).

C-Term/C-Term-GFP

The C-term of Unc13 (1647- 2871 aa) was amplified from cDNA clone LD28927 (obtained from DGRC, https://dgrc.bio.indiana.edu/Home) into pENTR/D-Topo (Invitrogen) using the following primers:

Unc13-Cterm-FW 5′- CACCATGCATCCCGGTGACAATCCATTC −3′
Unc13-Cterm-Rev 5′- TGTACCCATGGTTGGCTCCT-3′

Giving Rise to the Following Protein Sequence (1647-2871 aa)

HPGDNPFYSNIDSMPDIRPRRKSIPLVSELTMAATKRNAGLTSAVPRATLNDEDLKMHVYKKALQALIYPISSTTPHNFLLWTATSPTYCY
ECEGLLWGIARQGVRCTECGVKCHEKCKDLLNADCLQRAAEKSSKHGAEDKANSIITAMKDRMKQRREKPEIFELIRMTFGVDPDTHI
DSLEQAEHATVEGTSKWSCKLTITVICAQGLIAKDKSGTSDPYVTVQVSKVKKRTRTMPQELNPVWNEKFHFECHNSSDRIKVRVWDED
NDLKSKLRQKLTRESDDFLGQTIIEVRTLSGEMDVWYNLEKRTDKSAVSGAIRLHISVEIKGEEKVAPYHVQYTCLHENLFHYLCEENTG
MVKLPTQKGDDAWKLYFDEIPEEIVDEFSMRYGIENIYQAMTHFHCLSAKYLCPGVPAVMSTLLANINAYYAHTTASSAVSASDRFAASN
FGKEKFVKLLDQLHNSLRIDLSMYRNNFPASSPEKLMDLKSTVDLLTSITFFRMKVQELSSPPRASTVVKDCVKACLRSTYQFLFENCYE
LYNREFQVDPNEAKRAPDDHEPKLDSVDFWHKLIALIVSVIDEDKNSYGTVLNQFPQELNIGQLSASSMWHLFAVDMKYALEEHEQHRL
CKSSAYMNLHFRVKWLYSNYVKEVPPYKGAVPDYPAWFEPFVMQWLNENDDVSLEYLHGAFKRDKKDGFQKSSEHALFSNSVVDVF
TQLTQCFDVVSKLECPDPEIWKRYMRRFAKTIVKVLIAYADIVKLEFPEHMKDERIACILMNNIQQLRVQLEKMFESMGGDKLEEDAANI
LKELQQNLNSALDDLASQFAISLEPRITQSVRELGDMLLSIKGGSGTLAAGNLAAQRNAVAVEADEVLRPLMDLLDGSLTLYAQSCEKTV
LKRLLKELWKIVMRILEKTIVLPPMTDKTMMFKHLTDNAKNLASNAKIEDMGRLFKSHMAGKQDVKSALSGVMDISKEVEKNLSPKQCA
VLDVALDTIKQYFHAGGNGLKKTFLEKSPELQSLRYALSLYTQMTDTLIKTFISSQVHEVDLENSEESVGEISVQIDLFSHPGTGEHKVNV
KVVAANDLKWQIPSGMFRPFVDINLIGPHLQEKKRKFATKSKSNNWSPKYNESFSFTIGNEEQLDFFELHICVKDYCFARDDRLVGVAVIP
LKDISEKGSVACWLPLMRRIEMDETGWTILRILSQRNNDEVAKEFVKLKSEIRQEPTMGT.

Through Gateway reaction (Invitrogen, CA, UAS), the construct was shuttled into GAL4/UAS vector with or without C-terminal GFP tag.

For the generation of transgenic flies the construct was sent for DNA micro-injection into embryos to BestGene Inc, CA, USA using the PhiC31 integration system. The construct was inserted at the genomic position 75A10, 3L:17952108.17952108 (r6, Ti) (9725 fly strain; service type: H).

FL

To generate cDNA encoding Unc13A, the sequence encoding the C terminus of Unc13 (aa 1647−2871) was cloned from cDNA clone LD28927 (obtained from DGRC) into pENTR/D-Topo (Invitrogen, CA, USA) using the following primers:

Unc13-Cterm-FW, 5′-CACCATGCATCCCGGTGACAATCCATTC-3′,
Unc13-Cterm-Rev, 5′-TGTACCCATGGTTGGCTCCT-3′.

The sequence encoding a part of the Unc13A N terminus (lacking the first 1859 bp of Unc13A) is available at DGRC as cDNA with clone number LD15472. The sequence encoding the Unc13A C-terminal fragment was ligated to the sequence encoding the partial Unc13A N terminus (lacking the first 1859 bp). The obtained construct (Unc13-N+C) still lacked 1,859 bp of the N-terminal region of the whole Unc13A sequence. Therefore the missing fragment of Unc13-Isoform A/N-term (1-1859 bp) was cloned into pENTR/D-Topo vector using the following primers:

Unc13-1859 FW, 5′-CACCATGCGCACTACGTGAGGC-3′
Unc13-1859 REV, 5′-AGGCTTCAGATACTCAGATATG-3′.

In a final step, both fragments (Unc13-Isoform A/N-term (1-1859 bp) and Unc13-N+C) were fused in pENTR/D-Topo vector to gain the complete Unc13A cDNA. Through Gateway reaction, the construct was shuttled into GAL4/UAS vector. For the generation of transgenic flies the construct was sent for DNA micro-injection into embryos to BestGene Inc, CA, USA using the PhiC31 integration system. The construct was inserted at the genomic position 75A10, 3L:17952108.17952108 (r6, Ti) (9725 fly strain; service type: H).

Syx-1A-GFP

To generate cDNA encoding Syntaxin-1A, the sequence was amplified from cDNA clone LD43943 (obtained from DGRC) and cloned into pENTER-D-TOPO vector (Invitrogen, CA, USA) using the following primers:

Syntaxin_for 5′-CACCATGACTAAAGACAGATTAGCC-3′
Syntaxin_rev 5′-CATGAAATAACTGCTAACATATG-3′.

Through Gateway reaction (Invitrogen, CA, UAS), the construct was shuttled into GAL4/UAS vector with C-terminal GFP tag. For the generation of transgenic flies the construct was sent for DNA micro-injection into embryos to BestGene Inc, CA, USA using the PhiC31 integration system. The construct was inserted at the genomic position 75A10, 3L:17952108.17952108 (r6, Ti) (9725 fly strain; service type: H).

Unc18-GFP

To generate cDNA encoding Unc18, the sequence was amplified from cDNA clone SD04216 (obtained from DGRC) and cloned into pENTER-D-TOPO vector (Invitrogen, CA, USA) using the following primers:

0805DO-rop-fw 5′- GTCTATACTAGTATGGCCTTGAAAGTGCT −3′
0805DO-rop-rev 5′- GTCTATGGTACCGTCCTCCTTCGAGAGAGAACT −3′

Through Gateway reaction (Invitrogen, CA, UAS), the construct was shuttled into GAL4/UAS vector with C-terminal GFP tag. For the generation of transgenic flies the construct was sent for DNA micro-injection into embryos to BestGene Inc, CA, USA using the PhiC31 integration system. The construct was inserted at the genomic position 75A10, 3L:17952108.17952108 (r6, Ti) (9725 fly strain; service type: H).

Unc13A-RNAi

The Unc13A-RNAi was generated following the Harvard Medical School TRIP protocol (https://fgr.hms.harvard.edu/files/fly/files/2ndgenprotocol.pdf) using the following primers:

5′- CTAGCAGTGGGTTAGGACATAATAATCTATAGTTATATTCAAGCATATAGATTATTATG
TCCTAACCCGCG −3′
5′- AATTCGCGGGTTAGGACATAATAATCTATATGCTTGAATATAACTATAGATTATTATG
TCCTAACCCACTG-3′

Constructs were cloned into the pWalium20 vector. For the generation of transgenic flies the construct was sent for DNA micro-injection into embryos to BestGene Inc, CA, USA and injected into y[1] w[1118]; PBac{y[+]-attP-9A}VK00027 (Bloomington strain #9744).

Generation of Unc13 CaM^{W1620R,W1622R} Mutant

The Unc13 CaM mutant was generated by Red/ET recombineering based on the *unc13B^{null}* P[acman] clone (Böhme et al., 2016). In the region of the Unc13A CaM binding site (1615′ TARQRRHRAYNKIIMQLN 1632′aa) two point mutations were inserted by elongase-PCR using the following primers:

CaM mutation fw primer: 5′-CAGCTCGGCAACGACGGCATCGGGC-3′
CaM mutation rv primer: 5′-GCCCGATGCCGTCGTTGCCGAGCTG-3′

This induced an amino acid change at position 1620aa (W > R) and 1622aa (W > R).

For the generation of transgenic flies, the construct was sent for DNA microinjection into embryos to Rainbow Transgenic Flies, CA, USA (service type: B/D2, injected fly strain: strain 24862; y[1] M{vas-int.Dm}vZH-2A w[*]; PBac{y[+]-attP-9A}VK00005) on LB agar.

MHC-myrGCaMP5G

pBI-MHC-myrGCaMP5G was generated exchanging the UAS cassette of UAS-myrGCaMP5G (containing an Src64 myristoylation sequence; Melom et al., 2013) with the *Drosophila* myosin heavy chain promoter (1047 bp total, covering chromosome 2L positions 16766283 to 16767149 (GenBank sequence ID AE014134.6), synthesized at Eurofins Genomics, Germany) containing unique *SphI* and EcoRI restriction sites. The construct was then used for injection into *Drosophila* embryos for PhiC31-mediated genomic integration on the third chromosome (fly line 24862; y[1] M{vas-int.Dm}vZH-2A w[*]; PBac{y[+]-attP-9A}VK00005; Rainbow Transgenic Flies, CA, USA).

Generation of Unc13C-Term Antibody

A rabbit polyclonal antibody was raised against the C-term of Unc13. The antibody recognizes an epitope that is present in both Unc13 isoforms (A and B) with the following sequence:

YPAWFEPFVMQWLNENDDVSLEYLHGAFKRDKKDGFQKSSEHALFSNSVVDVFTQLTQCFDVVSKLECPDPEIWKRYMRRFAKTIV KVLIAYADIVKLEFPEHMKDERIACILMNNIQQLRVQLEKMFESMGGDKLEEDAANILKELQQNLNSALDDLASQFAISLEPRITQSVRELG DMLLSIKGGSGTLAAGNLAAQRN.

The PCR amplification of the DNA fragments was performed using the following primers

HB-UB2 FW 5′-CAGAATTCTACCCAGCATGGTTCGAG-3′
HB-UB2 REV 5′-TAGCGGCCGCTCAGTTCCTTTGAGCTGCA-3′

The construct was cloned to the bacterial expression vector Pgex-6p1 (GST tagged) and *E. coli* was used as expression host. The purified GST fusion protein (GST-Unc13C-term) was injected into a rabbit and the antiserum was affinity purified with the 6xHis-Unc13C-term fusion protein.

Immunostaining

Larvae were dissected and stained as described previously (Qin et al., 2005). The following primary antibodies were used: guinea-pig Unc13A (1:500; Böhme et al., 2016); mouse Syx-1A 8C3 (1:40; Developmental Studies Hybridoma Bank, University of Iowa, Iowa City, IA, USA; AB Registry ID: AB_528484); mouse Unc18/Rop 4F8 (1:500; Developmental Studies Hybridoma Bank, University of Iowa, Iowa City, IA, USA; AB Registry ID: AB_1157869); Unc13-C-term (1:500; this study); mouse GFP 3E6 (1:500, Thermo Fisher Scientific, MA, USA, A-11120; AB Registry ID: AB_221568), rabbit GFP (1:500, Thermo Fisher Scientific, MA, A11122; AB Registry ID: AB_221569), mouse Nc82 = anti-BRPC-term (1:200, Developmental Studies Hybridoma Bank, University of Iowa, Iowa City, IA, USA; AB Registry ID: AB_2314865); rabbit BRPLast200 (1:1000; Ullrich et al., 2015). Except for staining against Unc13A N-term (guinea pig), where larvae were fixed for 5 min with ice-cold methanol, all fixations were performed for 10 min with 4% paraformaldehyde (PFA) in 0.1 mM phosphate buffered saline (PBS). Secondary antibodies for standard immunostainings were used in the following concentrations: goat anti-HRP-Cy5 (1:250, Jackson ImmunoResearch, PA, USA); goat anti-rabbit-Cy3 (1:500, Jackson ImmunoResearch 111-165-144, PA, USA); goat anti-rabbit Cy5 (1:500, Jackson ImmunoResearch 111-175-144); goat anti-mouse-Cy3 (1:500, Jackson ImmunoResearch 115-165-146); donkey anti guinea pig DyLight 405 (1:500, Jackson ImmunoResearch 106-475-003, PA, USA); goat anti-mouse or anti guinea pig Alexa Fluor-488 (1:500, Life Technologies A11001/A11073, CA, USA). Larvae were mounted in vectashield (Vector labs, CA, USA). Secondary antibodies for STED were used in the following concentrations: goat anti-mouse Atto590 (1:100); goat anti-rabbit Atto590 (1:100); goat anti-guinea pig star635 (1:100); goat anti-rabbit star635 (1:100); Atto590 (ATTO-TEC AD 590-31) and star635 (Abberior 1-0101002-1) coupled to respective IgGs (Dianova). For STED imaging larvae were mounted in Mowiol (Max-Planck Institute for Biophysical Chemistry, Group of Stefan Hell).

Image Acquisition, Processing, and Analysis

Confocal microscopy was performed with a Leica SP8 microscope (Leica Microsystems, Germany). STED microscopy was performed with a custom-built STED-microscope (see below). Images of fixed and live samples were acquired at room temperature. Confocal imaging of NMJs was done using a z step of 0.25 μm (0.5 μm for GCaMP experiments). The following objective was used: 63 × 1.4 NA oil immersion for NMJ confocal imaging. All confocal images were acquired using the LAS X software (Leica

Microsystems, Germany). Images from fixed samples were taken from muscle four of 3rd instar larval NMJs (segments A2-A4). Images for figures were processed with ImageJ software to enhance brightness using the brightness/contrast function. If necessary, images were smoothened (0.5 pixel Sigma radius) using the Gaussian blur function. Confocal stacks were processed with ImageJ software (https://imagej.nih.gov/ij/). Quantifications of AZs (scored via BRP) were performed following an adjusted manual (Andlauer and Sigrist, 2012), briefly as follows. The signal of a HRP-Cy5 antibody was used as template for a mask, restricting the quantified area to the shape of the NMJ. The original confocal stacks were converted to maximal projections, and after background subtraction, a mask of the synaptic area was created by applying a certain threshold to remove irrelevant lower intensity pixels. The segmentation of single spots was done semi-automatically via the command "Find Maxima" embedded in the ImageJ software and by hand with the pencil tool and a line thickness of 1 pixel. To remove noise a Gaussian blur filter (0.5 pixel Sigma radius) was applied. The processed picture was then transformed into a binary mask using the same lower threshold value as in the first step. This binary mask was then projected onto the original unmodified image using the "min" operation from the ImageJ image calculator. The mean intensity of synaptic proteins per NMJ was measured using the command "measure" giving the mean gray pixel value within the HRP mask. For colocalization analysis (Manders or Pearson correlation) the ImageJ plugin "JACOP" (http://rsb.info.nih.gov/ij/plugins/track/jacop2.html) was used. To determine the active zone protein levels a custom-written ImageJ script was used. The ImageJ function "find maxima" was used to select high intensity pixels in the BRP channel marking AZ positions. The (x,y) positions of these were stored and then used to create a circle of size = 5 pixels centered around each (x,y) location. The integrated density within these ROIs was measured and taken for further calculations. For C-term-GFP, we excluded two NMJs that showed no expression of the protein.

STED Microscopy and Analysis

Two-color STED images were recorded on a custom-built STED-microscope (Göttfert et al., 2013), which combines two pairs of excitation laser beams of 595 nm and 640 nm wavelength with one STED fiber laser beam at 775 nm. All STED images were acquired using Imspector Software (Max Planck Innovation, Germany). STED images were processed using a linear deconvolution function integrated into Imspector Software (Max Planck Innovation, Germany). Regularization parameters ranged from $1e^{-09}$ to $1e^{-10}$. The point spread function (PSF) for deconvolution was generated by using a 2D Lorentz function with its half-width and half-length fitted to the half-width and half-length of each individual image. Images for figures were processed with ImageJ software to remove obvious background, enhance brightness/contrast and smoothened (1 pixel Sigma radius) using the Gaussian blur function. The average aligned intensity profiles depicted in Figure 1H were generated from STED images obtained by co-staining BRP together with either Unc13A, Syx-1 or Unc18. The BRP signal was used to align the local fluorescence signal in the following way: first, several sub-images (size 51 × 51 pixel, pixel size 10 nm) containing BRP rings were placed per STED images. The sub-images were cut out in both channels (BRP and either Unc13A, Syx-1A or Unc18) and centered according to the BRP signal. This was achieved by finding individual BRP peaks with the ImageJ (version 1.48q) function "find maxima," and shifting the image such that the center of gravity of the peaks was in the center of the sub-image. Only sub-images with at least two maxima were considered. To generate average fluorescence profiles, intensity line profiles were read out across a horizontal line in the middle of the image (pixels 1 to 51 in x at pixel position y = 26). The image was then successively rotated 35 times in 10° steps while reading out intensity profiles in the same manner. Intensity profiles of all rotations were averaged. This procedure was performed for all images in all channels (no. of sub-images for BRP/Unc13A: n = 132; no. of sub-images for BRP/Syx-1A: n = 117; no. of sub-images for BRP/Unc18: n = 134). Intensity profiles generated this way contained a local minimum at the center of the sub-images in all channels, demonstrating the proper alignment of the BRP signal and a stereotypical distribution of fluorescence. Intensity profiles were then plotted from the center outward and the midline pixel position (x = 26) was set to zero (no information is lost by this because intensity profiles were symmetric due to the averaging across full rotations of the individual images). To plot the mean fluorescence distribution across the plot area, mean absolute fluorescence values were divided by their peak values.

In order to align STED images of laterally viewed AZ stainings (BRP or RBP and various Unc13A epitopes (N-term; C-term; C-terminally GFP-tagged (FL-GFP))) and align signals from different AZs, we manually drew line ROIs through the center of the elongated BRP (or RBP) structure in all individual images (first channel) while leaving the second channel containing the Unc13A signal untouched. A third channel was added containing a line indicating the direction where the PM was situated by visual inspection. We then used a custom-written MATLAB (R2016a) script to determine the differences between the center coordinate of the line ROIs in the first channel and the center coordinate of the image in x and y dimension as described in Equations 1 to 4.

$$Sx = n^{-1} \cdot \sum_{1}^{n} x_{init}\ (n) \tag{1}$$

$$Sy = n^{-1} \cdot \sum_{1}^{n} y_{init}\ (n) \tag{2}$$

$$\Delta x = 25 - Sx \tag{3}$$

$$\Delta y = 25 - Sy \tag{4}$$

Here, (Sx,Sy) represents the center of mass of the (x,y)-coordinates in the initial line ROI, n is the number of points on the line (2 in all cases), and $x_{init}(n)$ and $y_{init}(n)$ are the positions of the n^{th} point on the current line ROI. All images in the three channels, as well as the coordinates of line ROIs in the first channel, were then translated by this determined (x,y)-difference (Δx/Δy; MATLAB function imtranslate) to align the center of the fluorescence profile with the center coordinate of the image space (51x51 px), arriving at the shifted line ROI coordinates $x/y_{centered}$ as described in Equations 5 and 6.

$$x_{centered}\,(n) = x_{init}\,(n) + \Delta x \tag{5}$$

$$y_{centered}\,(n) = y_{init}\,(n) + \Delta y \tag{6}$$

Subsequently, all images in all three channels (MATLAB function imrotate) and all line ROI coordinates (see Equation 7) were rotated around the center coordinate $x_{middle} = y_{middle} = 25.5$ by an angle α so that the coordinates of line ROIs in the first channel were congruent with the horizontal midline of the image space.

$$\begin{pmatrix} x_{rotated}\,(n) \\ y_{rotated}\,(n) \end{pmatrix} = \left[\begin{pmatrix} x_{centered}\,(n) \\ y_{centered}\,(n) \end{pmatrix} - \begin{pmatrix} x_{middle} \\ y_{middle} \end{pmatrix} \right] \cdot \begin{pmatrix} \cos(\alpha) & -\sin(\alpha) \\ \sin(\alpha) & \cos(\alpha) \end{pmatrix} + \begin{pmatrix} x_{middle} \\ y_{middle} \end{pmatrix} \tag{7}$$

Here, the resulting $x/y_{rotated}$ represents the points on the line ROIs after rotation by α. The angle α was determined by calculating the angle of the line ROI in the first channel to the horizontal midline. This was done by determining the lengths of opposite side and hypotenuse in a right triangle (squared Euclidean distance; MATLAB function pdist) made up of the midpoint (25.5,25.5), the first point on the line ROI (x_{ex},y_{ex}), and a point on the horizontal midline (x_{ex},25.5). The angle α in degrees resulted by calculating the inverse sine in radians (MATLAB function asind) as shown in Equation 8.

$$\alpha = \frac{\arcsin\left(\frac{l_{opposite}}{l_{hypotenuse}}\right) * 180^{\circ}}{\pi} \tag{8}$$

As the procedure so far did not regard the orientation of the AZ toward the PM, we then rotated every image in both channels by 180° in cases where the line ROI in the third channel was below the horizontal midline of the image. To generate a mean vertical intensity profile per AZ, the mean intensity of pixels was calculated for all rows. This was done for each AZ image individually. To align the intensity profiles of all AZs to the BRP signal, each profile was shifted such that the maximal intensity pixel was at 0. The same translation was then applied to the second channel. For the RBP/ FL-GFP staining, we used the intensity peak in the GFP staining as a reference. These were shifted such that all maxima were aligned and the same transition was performed on the RBP line profiles. To show the relative position of RBP with respect to the other stainings, these profiles were then shifted such that reference FL-GFP maxima overlapped with the mean position of the FL-GFP intensity peaks aligned to BRP. Finally, the average intensity profile of all AZs was calculated by averaging the profiles across all images and the SEM calculated. The profiles and SEM values were then divided by the maximum intensity value of the mean profile. The no. of sub-images was for BRP/Unc13A-N-term: n = 67; no. of sub-images for BRP/Unc13-C-term: n = 43; no. of sub-images for BRP/FL-GFP: n = 64; no. of sub-images RBP/FL-GFP: n = 26.

Electron Microscopy/HPF and Morphometric Analysis

HPF embedding was performed as described previously (Böhme et al., 2016; Matkovic et al., 2013). In brief, about three to five *Drosophila* late second/early third instar larvae were placed in aluminum specimen carrier of 200-μm depth (type A; Leica, Germany), filled with yeast paste, and covered with a lid (specimen carrier typeB, Leica, Germany). Samples were frozen immediately in an HPF machine (HPM100; Leica, Germany). Cryosubstitution was performed in an AFS (Leica, Germany) in anhydrous acetone with 1% EMD Millipore water, 1% glutaraldehyde, and 1% osmiumtetroxide. The sample was kept at −90°C overnight. Then the temperature was slowly (5°C/h) increased to −20°C, the samples incubated for additional 12 hr at this temperature before being warmed (10°C/h) to 20°C. The samples were washed with acetone and incubated with 0.1% uranylacetate dissolved in anhydrous acetone for 1 hr at room temperature. After washing, the samples were infiltrated with the plastic resin Epon in increasing concentrations. The first incubation step in 30% Epon/70% acetone for 4 hr was followed by 70% Epon/30% acetone overnight. The samples were incubated twice in 100% Epon for 2 hr before being embedded. 60–65 nm sections were cut using an ultramicrotome (RMC Power Tome XL; Reichert Ultracut S). Sections were collected on Formvar-coated 100 mesh grids. Sections were post-stained with 2% uranylacetate for 30 min and lead citrate for 3 min. Micrographs were acquired on an electrone microscope (Tecnai Spirit; FEI or Zeiss 900). The analysis of the EM micrographs was done with ImageJ. All EM analysis was performed blinded for genotypes using Fiji/ImageJ software. The micrographs were rotated (linear extrapolation) until the AZ membrane was horizontal. The PM, the electron-dense T-bar and SVs within a 300 nm radius from the T-bar center were detected by eye and labeled manually. For C-term-GFP morphometric analysis (Figure 5), the nearest distance of the outer leaflet of SVs to the inner leaflet of the PM at the T-bar pedestal center was measured manually. For experiments with overexpression of the N-term-GFP fragment (Figure 4), all SVs within each terminal were identified fitting them with a circle of 30 nm in diameter to determine the exact xy-center coordinates of each SV. We used these

xy-coordinates to measure the nearest neighboring distance to the T-bar center, defined as the center of the line interpolating the left and right edges of the T-bar pedestal touching the PM. Euclidean distances between pairs of xy-coordinates were determined with the MATLAB (R2016a) function pdist. From these distances, we subtracted 15 nm (SV-ROI radius) to estimate distances between SV outer leaflet and inner leaflet of the PM at the T-bar center. In all cases, SVs were categorized as "docked" by visual inspection. Only SVs without discernable distance between vesicular and PM were categorized as "docked." The SV distances to the T-bar pedestal center were binned in 30 nm bins (first bin centers: 25 nm for Figure 4Q, 15 nm for Figure 5Q) and the number of SVs in a respective bin was summed for all AZs and then divided by the number of investigated AZs (Figures 4Q and 5Q). To quantify minimal and maximal distances of docked SVs to the T-bar center per AZ, only SVs with distances < 135 nm were quantified for minimal distance and only SVs with distances > 135 nm were quantified to determine the average maximal distance. This was done to avoid counting the same SVs in both categories.

In Vivo Live Imaging and Analysis

In vivo imaging of intact *Drosophila* larvae was performed as previously described (Füger et al., 2007). Briefly, third instar larvae were put into a drop of Voltalef H10S oil (Arkema, France) within an airtight imaging chamber. Before imaging, the larvae were anaesthetized with 20 short pulses of a desflurane (Baxter, IL, UAS) air mixture until the heartbeat completely stopped. Selected NMJs were exclusively located in abdominal segments A2, A3 and A4 on muscles 26 and 27. For short-term FRAP (Syx-1A-GFP/Unc18-GFP/C-term-GFP/N-term-GFP; 270 s / 300 s) the NMJs were scanned with 700 Hz. The area supposed to be bleached (normally one bouton) was chosen and marked using the ROI function in the LCS AF software (Leica Microsystems, Germany). The ROI was chosen in a way that allowed having a bleached but also an unbleached internal control of intensity levels within one NMJ. Initially the NMJ was scanned for 10 s (before bleaching) to acquire the 100% intensity value. Subsequently, the laser intensity in the ROI was increased from ~3%–8% to 80% and the ROI bleached for 15 s. Then the laser intensity was reduced back to the original level and the NMJ was scanned until 270/300 s. Imaging was performed continuously, except for the N-term-GFP construct where single plane scans were imaged in 30 s intervals until 270 s. FRAP analysis was performed with ImageJ software. For short-term FRAP analysis (Figures 1 and 3), the integrated density of a background ROI outside the analyzed NMJ was subtracted from the integrated density of the bleached and also from an unbleached control ROI in the same NMJ for each acquisition time point. ROIs exhibited the same sizes. To account for unrelated fluorescence changes (e.g., bleaching or slight movement of the larvae), the data points were normalized to the fluorescence of the unbleached ROI by dividing the background-subtracted integrated density of the bleached ROI by the background-subtracted integrated density of the unbleached control ROI. The recovery was calculated as the normalized integrated density of the final time point (270/300 s) subtracted by the normalized intensity directly after the bleaching step. N-term-GFP analysis was performed as for FL-GFP. Recovery was calculated as the intensity at t = 270 s subtracted by the intensity shortly after photobleaching.

For long-term FRAP of FL-GFP a ROI within one NMJ was bleached. After image acquisition, single larvae were kept separately for 0.5, 1, 2, 4, 6 or 8 hr on normal food at 25°C. Subsequently, the same NMJs were subjected to live imaging again and the recovery in the bleached area was measured. For long-term FRAP analysis the mean intensity of the bleached ROI and an unbleached ROI of the same NMJ was measured and subtracted by the mean background intensity (outside the NMJ) for both time points, t = 0 (directly after bleaching) and each time point between 0.5 hr and 8 hr. The mean intensity was calculated by dividing the mean intensity of the bleached ROI by the mean intensity of the unbleached ROI. The recovery per NMJ was calculated as the intensity of the second time point (t = 0.5h-8h) subtracted by the intensity at t = 0 hr.

GCaMP Imaging, Immunostainings, and Activity Quantification

Larvae were raised on semi-defined medium (Bloomington recipe) at 25°C. Larvae were dissected (Qin et al., 2005) in ice-cold Ca^{2+}-free HL3 (Stewart et al., 1994); composition (in mM): NaCl 70, KCl 5, $MgCl_2$ 20, $NaHCO_3$ 10, trehalose 5, sucrose 115, HEPES 5, pH adjusted to 7.2. The Sylgard (184,Dow Corning, Midland, MI, USA) block containing the larva was transferred to a recording chamber containing HL3 with 1.5 mM $CaCl_2$ for imaging on an upright microscope (Olympus BX51WI) and imaging was performed using a water-immersion 60x objective (Olympus LUMFL 60x 1.10 w). The afferent motoneuron was sucked into a glass pipette which served as a stimulation electrode. The pipette was held in place by a patch electrode holder (NPI electronics) containing a chloride silver wire connected to a pipette holder (PPH-1P-BNC, NPI electronics) controlled by a micromanipulator (Narishige NMN25) which was connected to an S48 stimulator (Grass Technologies). A Sutter DG-4 (Sutter Instruments, Novato, CA, USA) served as a light source via a GFP filter set. The specimen was constantly illuminated during image acquisition for which an Orca Flash 4.0v2 sCMOS camera (Hamamatsu Photonics, Hamamatsu City, Japan) was used under control of the micro-Manager software (v1.4.20, https://micro-manager.org/). Imaging of GCaMP fluorescence in muscle 4 on abdominal segments 3 or 4 was performed over periods of 100 s (camera exposure time: 100 ms, acquisition rate 10 Hz) without stimulation to visualize spontaneous AZ activity (Figure 2; Figure S2). In the experiments shown in Figures 2 and S2, evoked activity was subsequently tracked over 180 s while stimulating the afferent nerve at 0.2 Hz. Voltage depolarizations of 6 V were applied for 300 μs to trigger action potentials and both the start of the camera acquisition and the timing of the stimulation were controlled by a software controlled (Clampex 10.5.0.9, Molecular Devices, CA, USA) amplifier/D-A/A-D converter (Digidata 1440A, Molecular Devices, CA, USA). For experiments depicted in Figure 1, only evoked activity was tracked (i.e., with no prior recording of spontaneous activity). The only difference here was that images were acquired with 50 ms exposure times and 20 Hz acquisition rate. In all cases, immunostaining following recordings was largely done as previously described (Muhammad et al., 2015). For all immunostainings against BRP and either Unc18, Syx-1A or

Unc13A, larval tissue was fixed immediately after recording in ice-cold methanol for 5 min. For details on antibodies and concentrations used, please refer to the above section on immunostaining.

While the drift-correction alignment of GCaMP recordings of larvae later stained for Unc18 and Syx-1A was performed as in Muhammad et al. (2015), the drift-correction alignment of videos taken from larvae later stained for Unc13A differed slightly. For this, we used the MATLAB (R2016a) function normxcorr2 (part of the 'Image Processing' toolbox) to find the x- and y-translation that yielded the maximum correlation coefficient between pairs of the first frame and subregions of all individual succeeding frames of the movie (similar to what has been described in Newman et al., 2017). The subregion of succeeding frames to be compared to the first frame was chosen before execution of the alignment code and included the whole NMJ (as determined by GCaMP fluorescence signal), and was identical for all frames of one recording. The function normxcorr2 returns a 2D array of values indicating the correlation coefficient between two compared images for every possible overlapping position relative to each other. The x,y-shift was then found by calculating the x,y-difference between the position of the second image (which was a subregion of all the frames following the first) and the position of the maximum value in the 2D array. All frames were Gaussian filtered (MATLAB function imgaussfilt) with an input sigma value of 5. To correct for changes in NMJ orientation and size, as well as uniform shearing in x- or y-direction related to fixation by Methanol or PFA, confocal images of the GCaMP channel in the fixed larvae were aligned to the first frame of the live GCaMP video using ImageJ (Fiji v1.49t). Three points were selected in corresponding locations of each respective image, and an affine transformation (allowing translation, rotation, and x/y-shearing) was carried out using the plug-in "TurboReg" (Biomedical Imaging Group, EPFL, Switzerland). If sufficient alignment could not be achieved, we used 4 reference points and performed a bilinear transformation (only necessary in 3 NMJs). The transformation determined for the GCaMP channel was then applied to all other channels (BRP and either Unc18, Unc13 or Syx-1A). ROIs with 650 nm diameter were then centrally overlaid with all BRP-positive spots as determined by the "find maxima" function of ImageJ with thresholds between 10 and 20. The integrated density of all confocal channels and the GCaMP video was read out in these ROIs. GCaMP Fluorescence values were read out as a function of time within each ROI. Additionally, to correct the GCaMP signal for non-specific background, for each GCaMP video the ROIs were shifted in x,y-dimension so that no ROI would overlay with an area of GCaMP signal. These shifted ROIs were used to measure the background in all frames of the GCaMP video, which was then subtracted from the intensity values measured in the original ROIs. This resulted in a time-dependent GCaMP fluorescence signal for each AZ, which was further analyzed.

Single synapse activity was then quantified by detecting peaks in the fluorescence trace in custom written MATLAB code. For this, the fluorescence trace was 1D-filtered (MATLAB function "filter") with a filter width of 5 frames for videos acquired with 20 Hz and a filter width of 3 frames for videos acquired with 10 Hz. To detect peaks in the fluorescence that mark postsynaptic activation of glutamate receptors the time-dependent fluorescence profile at each AZ location was inspected. Signals were considered only if the average fluorescence value in three subsequent frames exceeded a threshold which was chosen to be four times the value of the standard deviation of the signal. Since the spatial dimensions of the GCaMP fluorescence – especially for large signals – can exceed the inter-AZ distance, we ensured the assignment of activity to a single AZ by only taking into account the ROI with maximal signal intensity and not considering ROIs within a circular area of 2.5 μm radius. Finally, all signals matching these criteria were checked by visual inspection. To classify spontaneous activity, all events were considered. When evoked activity was tracked, the analysis was limited to peaks occurring within 1 s of stimulation to ensure relation to the AP.

To generate activity maps of spontaneous and evoked GCaMP signals (Figure 2B; Figure S2A), we used the number of signals per single AZ derived from the analysis described above, and plotted colored circles with sizes corresponding to the number of signals over an inverted BRP immunostaining of the recorded NMJ. Average fluorescence traces of spontaneous and evoked events were determined from averages of all signals in the respective release mode on one NMJ and then averaged over all animals. Exemplary single events corresponding to individual AZs were taken from the raw 8-bit GCaMP video and overlaid with a 16-color LUT in ImageJ, and optimized for contrast (Figure 1J).

To relate single AZ activities to the local levels of different proteins (BRP; Unc13A N-term; Figures 1K and 1L; Figure S2C), Unc18, and Syx-1A) (as shown in Figures 1K, 1L, and 2E), the fluorescence intensities in the same ROIs that were used to read out the GCaMP signal were used to read out the integrated density in the different channels (i.e., AZ-wise). Fluorescence intensities for all channels were read out in selected ROIs for Figure 2A. For analyses shown in Figures 1 and S2 (where multiple proteins were compared) intensities were maximized for range and normalized by first subtracting the minimum of all AZ intensity values in one NMJ from all AZ intensity values, and then dividing by the maximum value, yielding values between 0 and 1. This was not necessary in the analysis depicted in Figures 2E and 2F, where only a single staining (BRP) was analyzed and there the raw intensity values were used which also allows comparison of genotype-specific differences after Unc13A RNAi knockdown. In all cases AZs were then categorized by their fluorescence in the immunostaining. Signals were sorted in ascending order of intensity and categorized into 4 bins (each bin contained the same number of AZs). Within each bin, the average fluorescence intensity was calculated. Then the average activity at the AZs within each bin was calculated. Only one NMJ was recorded per animal. The activity and the intensity levels of the immunostaining were averaged over all animals.

To investigate whether AZs specialized for either evoked or spontaneous transmission, we used recordings in which both activities were recorded from the same set of AZs. In all cases, spontaneous recordings preceded ones with stimulation. Then, for each animal the number of AZs in each category (silent: neither evoked nor spontaneous release, mixed: at least one spontaneous and at least one evoked event, evoked only or spontaneous only) was counted and divided by the total number of AZs. The fraction of AZs within each category was then averaged over all animals.

Our experimental setup and analysis differ slightly from that of Peled and colleagues (Peled et al., 2014), as we used GCaMP5 (instead of GCaMP3), and measured spontaneous release before we recorded evoked release (as opposed to measuring spontaneous release within 15 s intervals between stimulating the nerve). Furthermore, we only looked for spontaneous or evoked events at intensity maxima of BRP in immunostainings. These factors may be an influence on the differing outcome of our analysis of spontaneous release. However, we think of the differing genotype as the major contributing factor.

Electrophysiology

Two-electrode voltage clamp (TEVC) recordings were performed essentially as previously described (Qin et al., 2005). All experiments were performed on male, third-instar larval NMJs (muscle 6 of abdominal segments A2/A3), raised on semi-defined medium (Bloomington recipe) at 25°C. Larvae were dissected in Ca^{2+}-free hemolymph-like solution (HL3; Stewart et al., 1994; composition (in mM): NaCl 70, KCl 5, $MgCl_2$ 20, $NaHCO_3$ 10, trehalose 5, sucrose 115, HEPES 5, pH adjusted to 7.2). Except where noted otherwise, the extracellular solution was HL3 containing 1.5 mM $CaCl_2$. Recordings were only further considered from cells with an initial V_m between −50 and −70 mV and input resistances of $\geq$ 4 MΩ, using intracellular electrodes with resistances of 8-15 MΩ, for Figure S5 at 15- 30 MΩ, filled with 3 M KCl. eEJCs and mEJCs were recorded at a clamped voltage of −70 mV. eEJCs were low-pass filtered at 5 kHz and sampled at 10 kHz, for Figure S5 at 20 kHz. Paired pulse ratios were calculated by dividing the amplitude after the second stimulus by the amplitude after the first stimulus. Only the synchronous component of the second response was considered. This was calculated by subtraction of the remaining asynchronous component (remaining current before downstroke) of the preceding eEJC. High-frequency stimulation experiments in Figure S8 30 APs were stimulated at 100 Hz (HL3 with 1.5 mM $CaCl_2$). To calculate the synchronous release component, responses were first baseline corrected. All stimulation artifacts were removed by connecting traces immediately before and after the artifact with a line. Total amplitudes were calculated as the peak current values after each stimulus, synchronous release was calculated by subtracting the remaining asynchronous current of the preceding stimulus. Each response amplitude of the train was then divided by the mean mEJC amplitude to determine number of quanta released per AP. The cumulative quantal content was plotted against the stimulus number and a linear regression line was fit to the last 5 data points. The slope and Y-intercept of the back-extrapolation (linear regression) line was estimated in each cell. Time-to-peak was calculated using Clampfit 10.3 (Molecular Devices, CA, USA) (Figure S5). For illustration purposes in Figure S5A example mini traces were resampled using MATLAB (R2016a) function resample with input 1:4.

Variance-mean experiments were performed from an initial Ca^{2+} concentration of 0.75 mM. The concentration was subsequently increased to 1.5, 3.0, and 6.0 mM for N-term-GFP and controls. For FL-GFP and C-term-GFP an additional concentration of 12 mM was used. In Figures 4J–4L, 15 eEJCs (stimulated at 0.2 Hz) were recorded at each Ca^{2+} concentration. Following the stimulation, the bath solution was exchanged five times via pipetting, a 30 s acclimation period was given, and the process was repeated at the next Ca^{2+} concentration. In Figures 5J–5L a peristaltic pump (Gilson Minipuls 3) was used to exchange the bath solution. The muscle was stimulated at 0.2 Hz for the entire duration of the experiment. After 20 eEJCs had been recorded, the pump was activated and the eEJCs during the transition phase were also recorded. When the bath solution had been completely exchanged, 20 eEJCs were recorded at the new Ca^{2+} concentration. To obtain the plots in Figures 4K and 5K, response amplitudes were averaged at each Ca^{2+} concentration and then plotted against the mean variance of the amplitudes (Standard Deviation squared $(SD)^2$). Using GraphPad Prism v5.01, the data were fit with a standard parabola ($SD^2 = q^*\bar{I} - \bar{I}^2/N$), where q is the quantal size, $\bar{I}$ is the mean current amplitude, and N is the number of release sites. N was calculated cell-wise in Figures 4L and 5L: from parabola fits to individual recordings. The parabolas shown in Figures 4K and 5K are fits to the full dataset, taking individual values into account using the built in curve fitting function of GraphPad Prism v5.01. Akaike's information criterion was determined using the implemented function in GraphPad Prism v5.01.

Ca^{2+} Buffering with EGTA-AM (TEVC)

In an incubation experiment, EGTA-AM (Calbiochem, 50 mM stock solution in DMSO) was dissolved in Ca^{2+}-free HL3 to a final concentration of 0.1 mM. The same volume of Pluronic F-127 (Molecular Probes, 20% (w/v) in DMSO) was added, leading to a final Pluronic concentration of 0.04% (w/v). For control cells, EGTA-AM was replaced by an equal amount of DMSO. The dissected larva was incubated exactly 30 min at room temperature, then rinsed three times with HL3 containing 2.5 mM Ca^{2+} to remove residual EGTA-AM from the fillet before the recording was started. In two-electrode voltage clamp eEJCs during a 101 AP-train at 60 Hz train were measured at −60 mV in HL3 with 2.5 mM Ca^{2+}, data were analyzed using pClamp 10 (Molecular Devices, Sunnyvale, CA, USA) and a custom-written MATLAB (MathWorks, R2010b) script.

Trains were baseline corrected to the beginning of the trace prior to initiation of stimulation. All stimulation artifacts were removed by connecting samples immediately before and after the artifact by a line. Trains depicted in Figures 6 and S7 are averages from all cells recorded. Total amplitudes were calculated per cell as the peak amplitude after each stimulus. Asynchronous amplitudes were calculated in each cell as the current, prior to the downstroke related to the following stimulus. Synchronous amplitudes were calculated as the difference of the current at the beginning of a stimulus and the total peak amplitude of the stimulus. Paired pulse ratios were calculated as the second synchronous amplitude divided by the first synchronous amplitude in a train. Time-to-peaks were calculated as the time from the beginning of each stimulus to the total amplitude.

QUANTIFICATION AND STATISTICAL ANALYSIS

Data were analyzed using Prism (GraphPad Software, CA, USA). To compare two groups, two tailed t tests or Mann-Whitney U tests were used for all datasets. For comparison of more than two groups, one-way analysis of variance (ANOVA) tests were used, followed by a Tukey's multiple comparison test. p values and N values are given in the Table S1. Means are annotated ± SEM. Asterisks are used to denote significance: *, $p < 0.05$; **, $p < 0.01$; ***, $p < 0.001$; n.s. (not significant), $p > 0.05$.

DATA AND SOFTWARE AVAILABILITY

The MATLAB and ImageJ codes used in this study are available from A.M.W. upon request.

Neuron, Volume *95*

Supplemental Information

Stable Positioning of Unc13 Restricts Synaptic Vesicle Fusion to Defined Release Sites to Promote Synchronous Neurotransmission

Suneel Reddy-Alla, Mathias A. Böhme, Eric Reynolds, Christina Beis, Andreas T. Grasskamp, Malou M. Mampell, Marta Maglione, Meida Jusyte, Ulises Rey, Husam Babikir, Anthony W. McCarthy, Christine Quentin, Tanja Matkovic, Dominique Dufour Bergeron, Zeeshan Mushtaq, Fabian Göttfert, David Owald, Thorsten Mielke, Stefan W. Hell, Stephan J. Sigrist, and Alexander M. Walter

Inventory of supplemental information

Movie 1: live movie of GCaMP fluorescence – related to Figure 1

Movie 1 shows a 34 s excerpt from a stabilized GCaMP recording in real time in which action potentials were evoked. Data like these were used for Figures 1I-L; 2 and S2.

Figure S1 – related to Figure 1

Figure S1 provides long-term FRAP analysis of motoneuronally overexpressed Unc13A-GFP and thus complements the short-term FRAP data of Figure 1M-Q.

Figure S2 – related to Figure 2

Figure S2 shows GCaMP-based single active zone measurements of spontaneous and evoked activity in correlation to levels of BRP and Unc13A and complements the data shown in Fig 2.

Figure S3 – related to Figure 3

Figure S3 provides confocal and STED analysis of motoneuronally overexpressed N-term-GFP as well as C-term-GFP and thus complements the analysis provided in Figure 3C-F.

Figure S4 – related to Figure 4

Figure S4 shows that the overexpression of the N-term-GFP fragment displaces endogenous Unc13 from the AZ. These data help to interpret the reduced number of release sites shown in Figure 4K,L.

Figure S5 – related to Figure 5

Figure S5 shows the effect of mutating the CaM-binding site of Unc13A on synaptic transmission. This mutation does not phenocopy the effects observed upon rescue with the C-term-GFP fragment, suggesting that loss of the CaM domain in the C-term-GFP is not causative for the effects observed in Figure 5.

Figure S6 – related to Figure 5

Figure S6 shows that expression of the C-term-GFP fragment in the *unc13*^{null} background redistributes RBP, but neither Syx-1A nor Unc18 from the AZ and characterizes an additional phenotype of this genotype.

Figure S7 – related to Figure 6

Figure S7 shows the full 60 Hz trains of C-term-GFP rescue with and without EGTA as in Fig. 6 only the responses to the first 20 APs are shown. Furthermore, Figure S7 also shows that the large facilitation observed in the C-term-GFP rescue (Figure 6C) was mainly caused by an increase in the asynchronous release component which could be inhibited by EGTA incubation.

Figure S8 – related to Figure 6

Figure S8 shows that a higher stimulation frequency of 100 Hz compared to the 60 Hz train investigated in Figures 6 and S7 further increased the contribution of asynchronous release and the delay in transmission. Furthermore, analysis with linear fits to cumulative responses reveals that *unc13*^{null} larvae expressing the C-term-GFP fragment have comparable back-extrapolated y-intercepts but slowed forward priming.

Table S1 – related to all figures including supplemental figures

Table S1 provides all Figure source data, number of experiments, P values and the nature of the statistical comparisons used in this study.

Supplementary figures and legends

Figure S1 – related to Figure 1

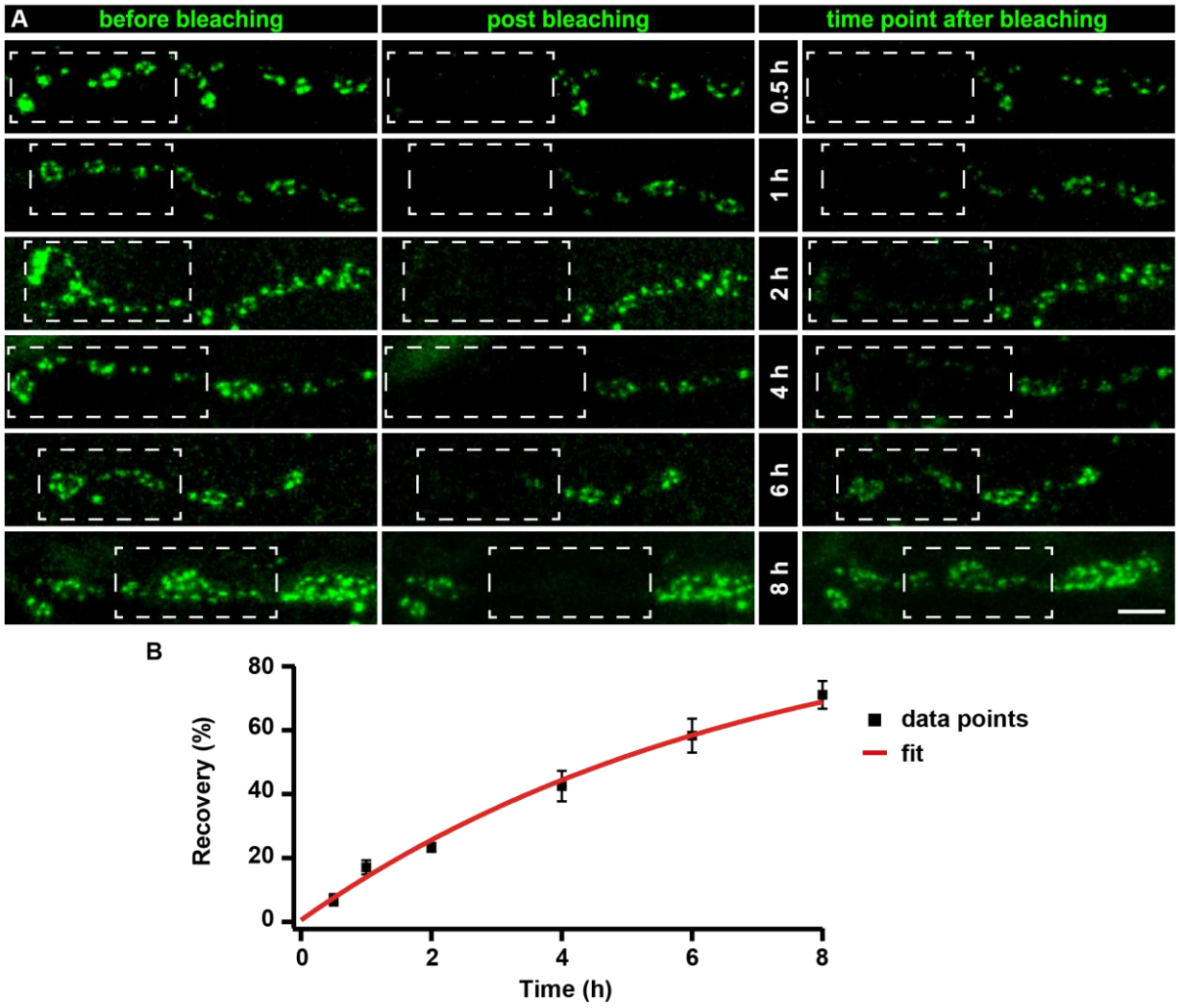

Figure S1: Unc13A recovers within hours

(A) Long-term FRAP of motoneuronally overexpressed Unc13A-GFP of muscle 26/27. Dashed box shows bleached bouton before and directly after the fluorescence bleaching. Fluorescence recovery was measured 0.5; 1; 2; 4; 6 or 8 h after bleaching. Different time points were measured in different animals. **(B)** Quantification of recovery (%) over time. Bleached Unc13A-GFP showed a slow fluorescence recovery, exhibiting a tau of 6.88 ± 0.55 h, single exponential recovery fit. Figure source data are listed in **Supplementary Table 1**. Data are mean ± s.e.m. Scale bar 5 µm.

Figure S2 – related to Figure 2

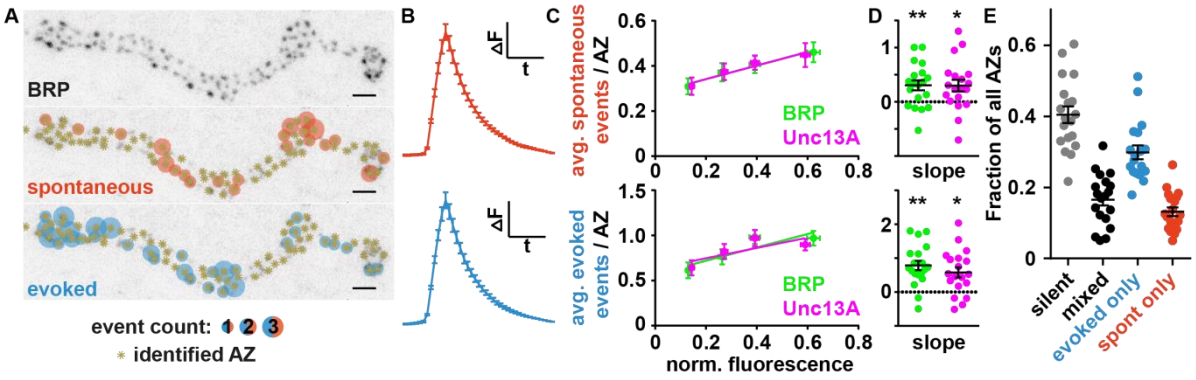

Figure S2: GCaMP-based single active zone measurements of spontaneous and evoked activity

(A) Inverted confocal image of BRP staining overlaid with asterisks to mark identified AZ positions and with circles corresponding to number of spontaneous/evoked events, measured in GCaMP experiments. **(B)** Average GCaMP fluorescence changes induced by spontaneous (top) and evoked (bottom) events at all imaged NMJs. (Average of all animals). **(C)** Top: average number of spontaneous events per AZ plotted against normalized, local fluorescence levels of BRP and Unc13A. Bottom: same for evoked events. **(D)** Slopes of linear fits on measurements in individual NMJs. Stars indicate statistically significant deviation from zero. **(E)** Quantification of release modes shown in all NMJs. Silent: no activity; mixed: both spontaneous and evoked activity; evoked/spont only: only one release mode observed. All panels show mean ± s.e.m. Figure source data, number of experiments and P values are listed in **Supplementary Table 1**. Scale bars: 2 µm.

Figure S3 – related to Figure 3

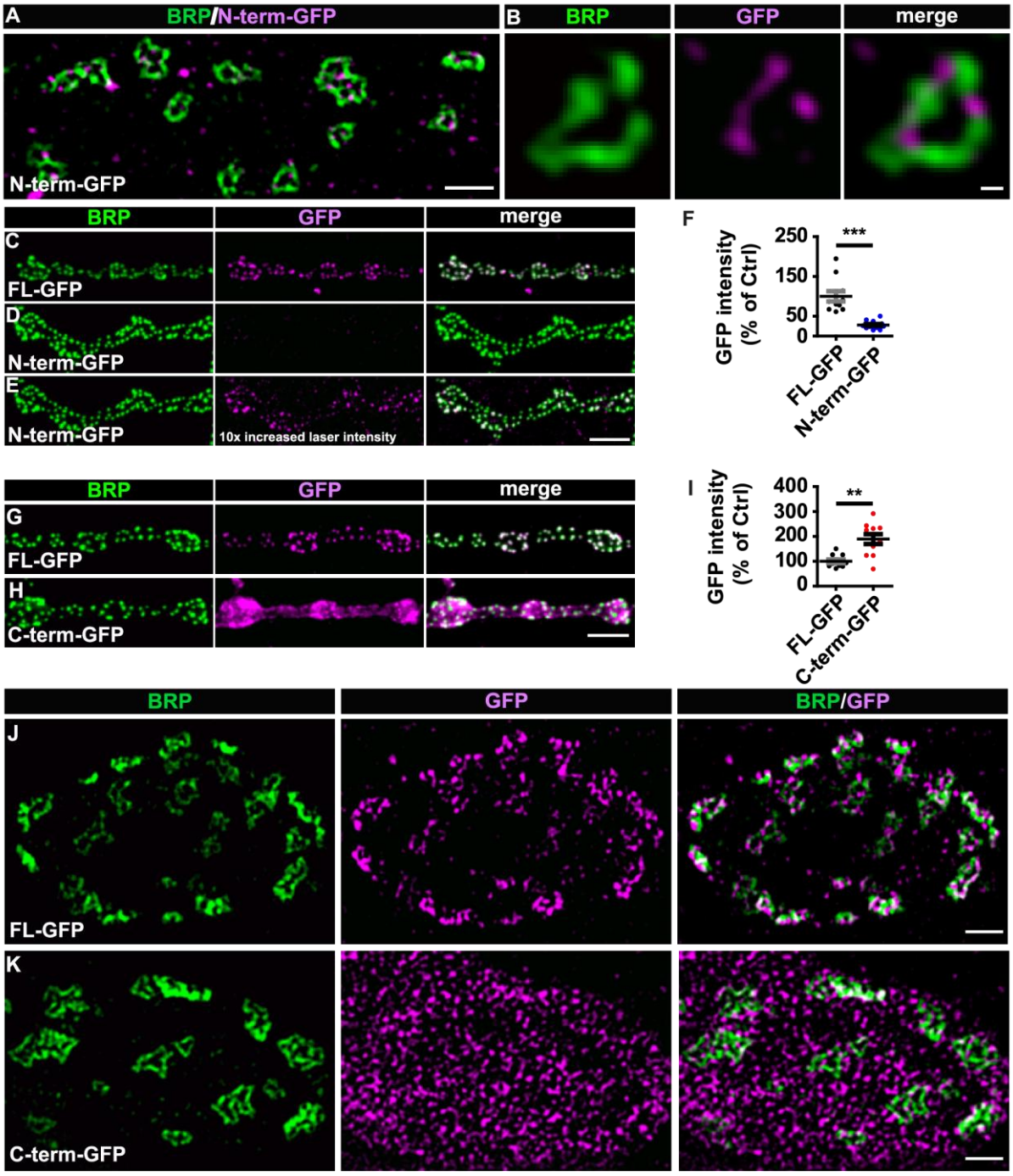

Figure S3: the N-term-GFP fragment but not the C-term-GFP fragment localized specifically to AZs

(A,B) Two-color STED image of synaptic bouton (A) and single AZs (B) from 3rd instar larvae pan-neuronally overexpressing N-term-GFP stained with the indicated antibodies. **(C-E)** Muscle 4 NMJs of segment A2-4 from 3rd instar Wild-type larvae pan-neuronally overexpressing FL-GFP (C) or N-term-GFP (D,E) labelled with the indicated antibodies. In (E) the laser intensity exciting the GFP staining was increased 10x in comparison to FL-GFP. **(F)** Quantification of GFP intensity measured over the whole NMJ in both conditions. **(G,H)** Muscle 4 NMJs of segment A2-4 from 3rd instar *unc13*^{null} larvae pan-neuronally expressing FL-GFP (G) or C-term-GFP (H) labelled with the indicated antibodies. **(I)** Quantification of GFP intensity measured over the whole NMJ in

both conditions. **(J,K)** Two-color STED image of a synaptic bouton from 3rd instar *unc13*^{null} larvae pan-neuronally expressing FL-GFP (J) or C-term-GFP (K) stained with the indicated antibodies. Figure source data, number of experiments and P values are listed in **Supplementary Table 1**. Scale bar: (A,J,K) 500 nm; (B) 50 nm; (C-E; G,H) 5 µm. Statistics (F,I): Mann-Whitney U test. $^{**}P \leq 0.01$; $^{***}P \leq 0.001$; ns, not significant, $P > 0.05$. All panels show mean ± s.e.m..

Figure S4 – related to Figure 4

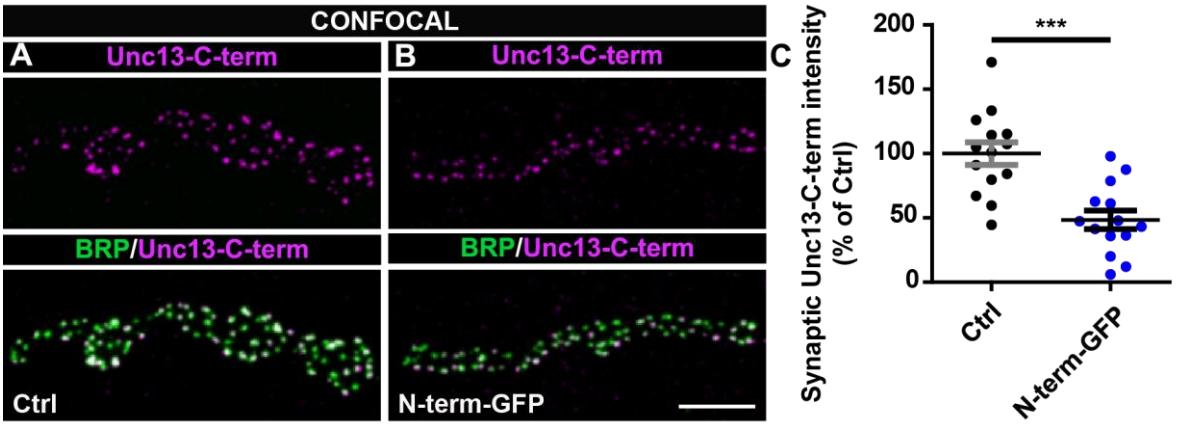

Figure S4: overexpression of N-term-GFP displaces endogenous Unc13 from the AZ

(A,B) Muscle 4 NMJs of segment A2-4 from 3rd instar larvae of Ctrl (A) and pan-neuronally overexpressing N-term-GFP (B) labelled with the indicated antibodies. **(C)** Quantification of synaptic Unc13-C-term intensity for Ctrl and pan-neuronally overexpressed N-term-GFP. Figure source data, number of experiments and P values are listed in **Supplementary Table 1**. Scale bar: 5 µm. Statistics: Mann-Whitney U-test. ***$P \leq 0.001$. Panel shows mean ± s.e.m.

Figure S5 – related to Figure 5

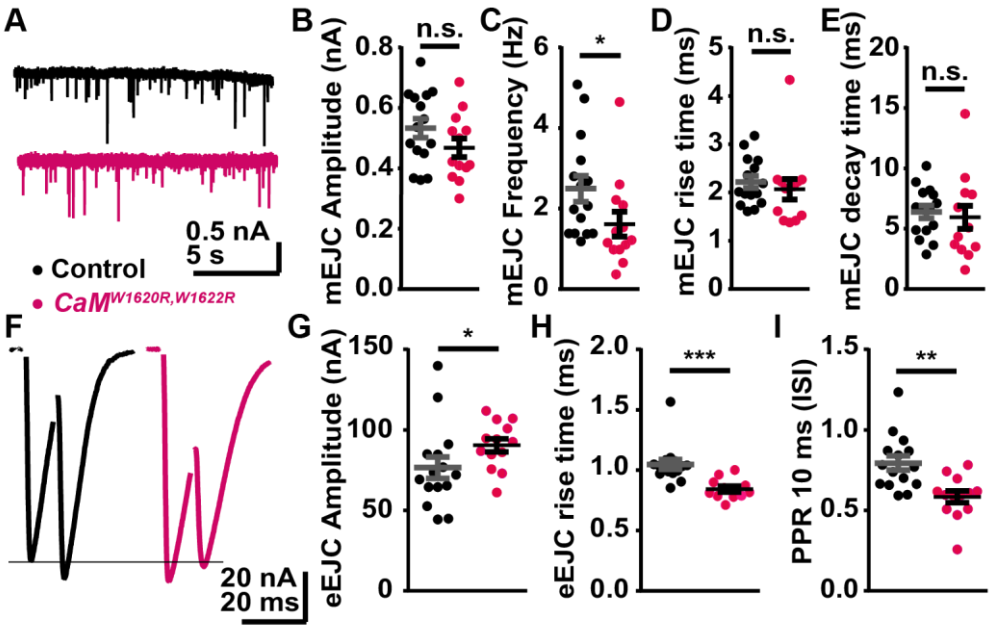

Figure S5: influence of CaM-binding site mutation in Unc13A on synaptic transmission

(A) Representative mEJC traces for Control (black) and *CaM*^{W1620R,W1622R} (magenta) cells. **(B-E)** mEJC amplitudes (B), frequencies (C), rise times (10% to 90%; (D)), and decays (E) in Control and *CaM*^{W1620R,W1622R}. **(F)** Representative eEJC traces for Control and *CaM*^{W1620R,W1622R} cells. **(G-I)** Quantification of eEJC amplitudes (G), rise times (10% to 90%; H)), and paired pulse ratios with 10 ms ISI (I) in Control and *CaM*^{W1620R,W1622R} cells. Figure source data, number of experiments and P values are listed in **Supplementary Table 1**. Statistics: Mann-Whitney U test. *P ≤ 0.05; **P ≤ 0.01; ***P ≤ 0.001; ns, not significant, P > 0.05. All panels show mean ± s.e.m.

Figure S6 – related to Figure 5

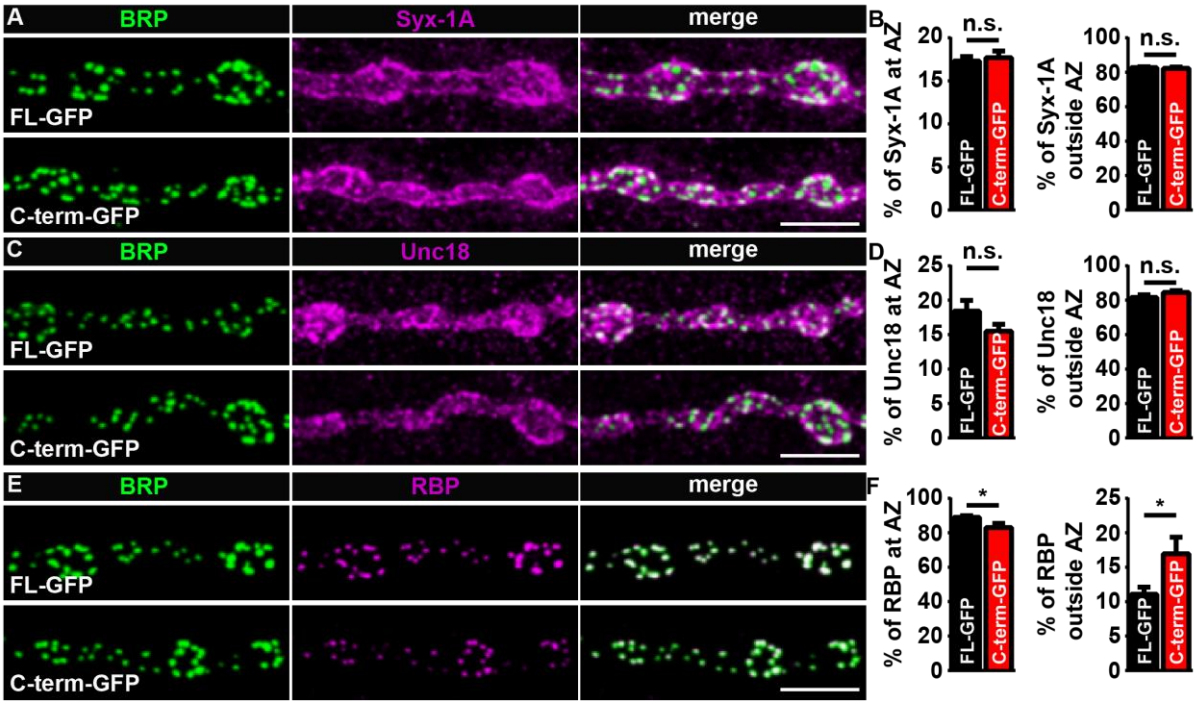

Figure S6: C-term-GFP redistributed RBP from the AZ

(A,C,E) Muscle 4 NMJs of segment A2-4 from 3rd instar *unc13*^{null} larvae pan-neuronally expressing FL-GFP or C-term-GFP labelled with the indicated antibodies. **(B,D,F)** Quantification of percentage of Syx-1A (B), Unc18 (D) and RBP (F) in- and outside of the AZ. Figure source data, number of experiments and P values are listed in **Supplementary Table 1**. Scale bar: 5 µm. Statistics: Mann-Whitney U-test. *$P \leq 0.05$; ns, not significant, $P > 0.05$. Panel shows mean ± s.e.m.

Figure S7 – related to Figure 6

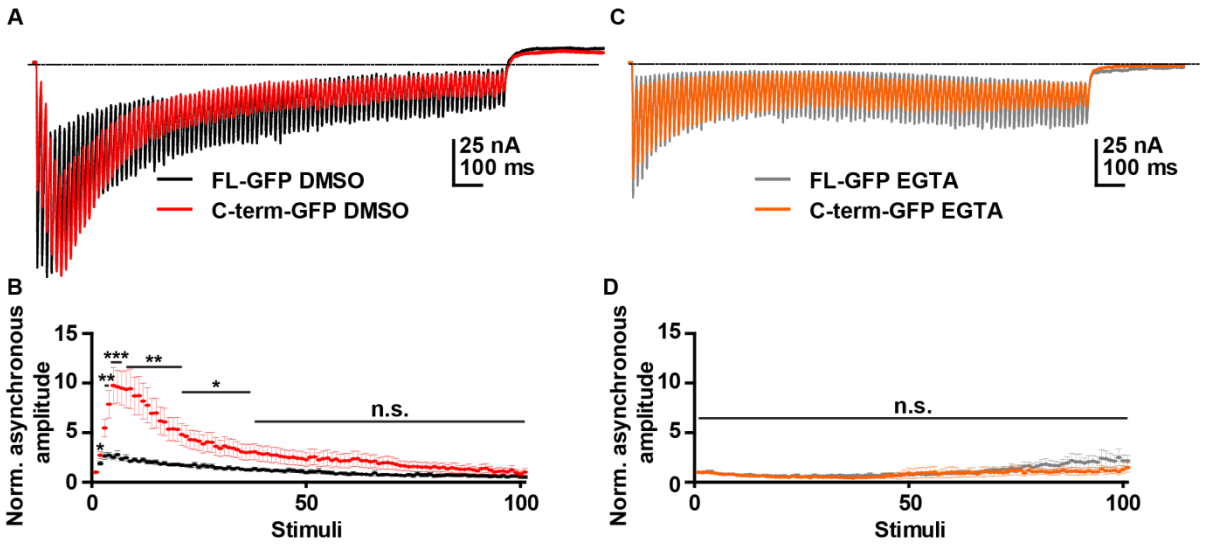

Figure S7: synaptic transmission upon rescue with C-term-GFP has augmented asynchronous release which is abolished by EGTA treatment

(A) Average eEJC traces of *unc13*^{null} larvae expressing FL-GFP (control, black) or C-term-GFP (red) in the absence of EGTA in response to 60 Hz trains (extended view of traces in Figure 6A, here showing all responses). **(B)** Normalized asynchronous amplitude plotted against stimulus number without EGTA in both genotypes. **(C)** Average eEJC traces for FL-GFP (control, grey) and C-term-GFP (orange) expressing *unc13*^{null} larvae in the presence of EGTA in response to 60 Hz trains (extended view of traces in Figure 6G, here showing all responses). **(D)** Normalized asynchronous amplitude plotted against stimulus number for FL-GFP and C-term-GFP in the presence of EGTA. Figure source data, number of experiments and P values are listed in **Supplementary Table 1**. Statistics: t test. *$P \leq 0.05$; **$P \leq 0.01$; ***$P \leq 0.001$; ns, not significant, $P > 0.05$. All panels show mean ± s.e.m. The extracellular solution contained 2.5 mM Ca^{2+}.

Figure S8 – related to Figure 6

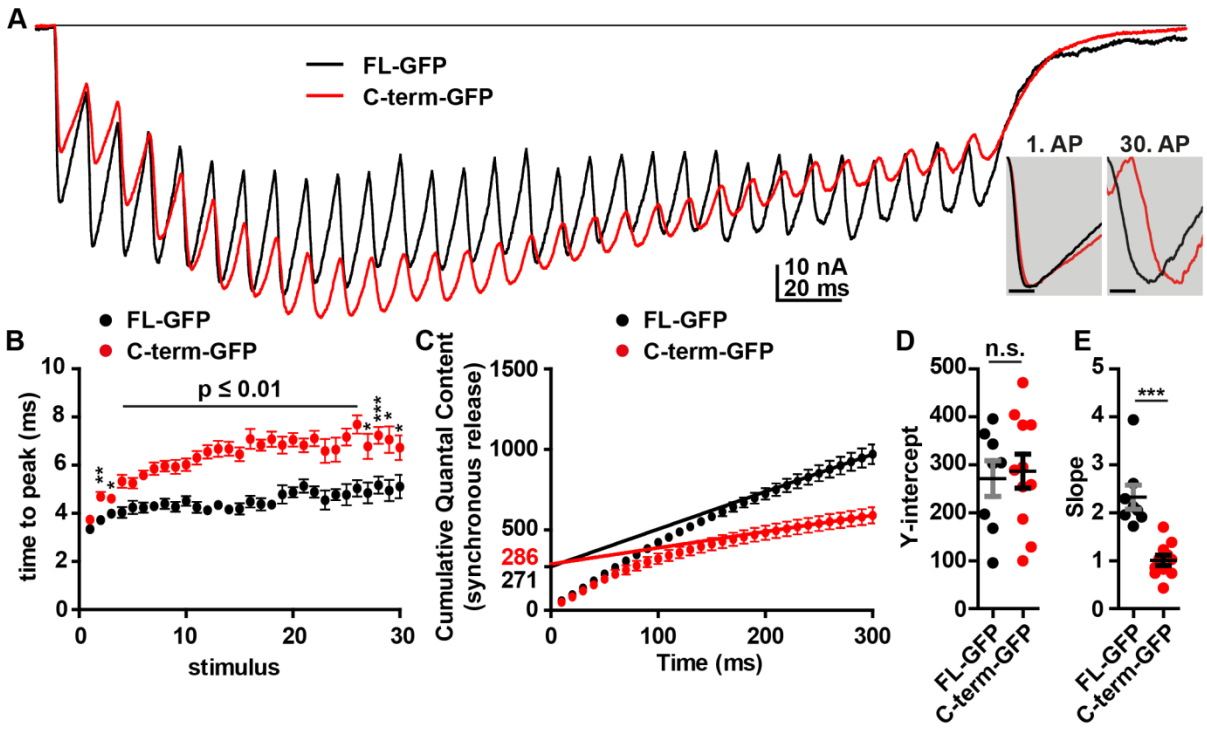

Figure S8: asynchronous and delayed release and slower forward priming in *unc13*^{null} larvae expressing the C-term-GFP fragment

(A) Average eEJC traces of *unc13*^{null} larvae expressing FL-GFP (control, black) or C-term-GFP (red) in response to 100 Hz trains, 30 APs. Inlets show average, normalized eEJC amplitudes to the first stimulus and to the 30th stimulus of FL-GFP (black) and C-term-GFP (red) expressing cells to illustrate effects on the time course of release. **(B)** Time-to-peak (ms) for FL-GFP (control, black) and C-term-GFP (red) conditions plotted against stimuli number. **(C)** Cumulative quantal content (synchronous release divided by mean mEJC amplitudes in each genotype) plotted against time (ms) in both genotypes. Lines represent the best fit to all data in each genotype, fits restricted to 260-300 ms. **(D)** Cell-wise quantification of y-intercepts from linear fits from individual cells of either genotype. **(E)** Cell-wise quantification slopes of linear fits in individual cells of either genotype. The slope was significantly larger in FL-GFP compared to C-term-GFP. Figure source data, number of experiments and P values are listed in **Supplementary Table 1**. Statistics: t test. *$P \leq 0.05$; **$P \leq 0.01$; ***$P \leq 0.001$; ns, not significant, $P > 0.05$. All panels show mean ± s.e.m.. The extracellular solution contained 1.5 mM Ca^{2+}.